Acta Astronautica 191 (2022) 374–393

Contents lists available at ScienceDirect

Acta Astronautica

journal homepage: www.elsevier.com/locate/actaastro

Research paper

Air-breathing electric propulsion: Flight envelope identification and development of control for long-term orbital stability

M. Tisaev [a,*], E. Ferrato [b], V. Giannetti [b], C. Paissoni [b], N. Baresi [a], A. Lucca Fabris [a], T. Andreussi [b]

[a] Surrey Space Centre, University of Surrey, Guildford, UK
[b] SITAEL S.p.A., Pisa, 56121, Italy

ARTICLE INFO

Keywords:
Air-breathing electric propulsion
ABEP
Frozen orbit
VLEO
AETHER

ABSTRACT

Air-breathing electric propulsion (ABEP) enables long duration missions at very low orbital altitudes through the use of drag compensation. A system-level spacecraft model is developed, using the interaction between thruster, intake and solar arrays, and coupled to a calculation of the drag. A quadratic solution is found for specific impulse and evaluated to identify the thruster performance required for drag-compensation at varying altitudes. An upper altitude limit around 190 km is based on a minimum thruster propellant density, resulting in required thruster performance values of $I_{sp} > 3000$ s and $T/P > 8$ mN/kW for a realistic ABEP spacecraft. The orbit of an air-breathing spacecraft is propagated with time, which highlights the prescribed orbit eccentricity due to non-spherical gravity and therefore an increased variability in the atmospheric conditions. A thruster control law is introduced which avoids a divergent altitude behaviour by preventing thruster firings around the orbit periapsis, as well as adding robustness against atmospheric changes due to season and solar activity. Through the use of an initial frozen orbit, thruster control and an augmented T/P, a stable long-term profile is demonstrated based on the performance data of a gridded-ion thruster tested with atmospheric propellants. An initial mean semi-major axis altitude of 200 km relative to the equatorial Earth radius, a spacecraft mass of 200 kg, $I_{sp} = 5455$ s and $T/P = 23$ mN/kW, results in an altitude range of around 10 km at altitudes of 160–183 km during a period of medium to high solar activity.

1. Introduction

Electric propulsion for spacecraft offers a high specific impulse, low-thrust profile that is ideal for drag compensation in very low Earth orbit (VLEO). However, a conventional xenon-based system is limited in lifetime by the use of on-board propellant. The air-breathing electric propulsion (ABEP) concept uses gases in the upper atmosphere as the propellant source for satellites in VLEO, broadly defined as orbital altitudes below 450 km [1]. The thrust produced by the propulsion system counteracts atmospheric drag, which typically causes rapid orbital decay, therefore allowing the use of orbits with a lower altitude than previously possible and a significant extension of the mission lifetime. If full drag compensation is achieved, an extended spacecraft life in VLEO is possible while the propulsion system continues to function as intended.

A long-duration satellite in VLEO is attractive for many applications, such as increased resolution or smaller required aperture size for Earth observation missions, the possibility for science missions to collect data on atmospheric properties and radiation, magnetic and gravitational fields at altitudes for which little data exists, and reduced latency for telecommunications satellites to achieve a fast connection to ground-based users [1]. Another advantage is the potential of reducing spacecraft launch mass by replacing conventionally heavy propellant tanks. This work is motivated by the AETHER (Air-breathing Electric THrustER) project, which is an initiative between European industry and research centres to build on the world-leading work of its members and develop a feasible system for the first ABEP spacecraft [2].

A detailed concept of an air-breathing ion engine was initially proposed in 2004 by Fujita [3,4] at JAXA, with particular focus on the design of an intake. The trade-off between a high mass flow to the thruster and also compression of the air to sufficiently high density was identified, and empirical fits were created to the data from Direct Simulation Monte-Carlo (DSMC) simulations. Initial estimates of the altitude range were found from spacecraft heating for the lower limit and propellant density for the upper limit. The procedure for both of these calculations is followed in this study. The minimum exhaust velocity required at different altitudes was identified using a simple formulation, that did not account for drag from deceleration of air due to the intake.

* Corresponding author.
E-mail address: m.tisaev@surrey.ac.uk (M. Tisaev).

https://doi.org/10.1016/j.actaastro.2021.11.011
Received 6 July 2021; Received in revised form 11 October 2021; Accepted 8 November 2021
Available online 20 November 2021

Nomenclature

α	Resultant angle of surface to u_∞
β (β_0)	Compression ratio (stagnation)
$\dot{m}$	Mass flow rate
ϵ	Speculative reflection fraction
ϵ_r	Reflectivity
η_{as}	Solar panel assembly efficiency
η_c	Collection efficiency
η_T	Total thruster efficiency
γ	Thrust correction
γ_h	Specific heat ratio
λ	Mean free path
μ	Dynamic viscosity
μ_E	Earth gravitational parameter
Ω	RAAN
ω	Argument of periapsis
ϕ	Spacecraft roll angle
ψ	Spacecraft yaw angle
ρ (ρ_0)	Density (stagnation)
σ	Diffuse reflection fraction
σ_{SB}	Stefan–Boltzmann constant
τ	Transmittance
Θ	True anomaly
θ, θ_a	Spacecraft and array pitch angle
ζ	Sub-system power factor
A	Area
a	Semi-major axis
A_{front}	Area perpendicular to flow
A_{par}	Area parallel to flow
A_p	Effective solar panel area
a_P	Array/panel specific power per unit area
Ap	Magnetic index
AR_i	Intake aspect ratio
AR_s	Spacecraft aspect ratio
c	Array length
C_{Df}^{cont}	Continuous regime shear drag coefficient
C_{Dp}^{cont}	Continuous regime pressure drag coefficient
C_D^{cont}	Continuous regime drag coefficient
C_D^{fmf}	Free-molecular drag coefficient
c_p	Specific heat capacity
CT	Control target
d	Molecular diameter
d_i	Intake diameter
e	Eccentricity
erf	Error function
$F10.7$	10.7 cm solar radio flux
F_D	Drag
F_T	Thrust
g_0	Gravity acceleration at sea level
H	Orbital altitude
h (h_0)	Specific enthalpy (stagnation)
i	Inclination
I_{sp}	Specific impulse
j	Surface index for resultant angle
k	Number of strip for side drag integration
k_B	Boltzmann constant
Kn	Knudsen number
L	Spacecraft length
M	Molar mass
m	Molecular mass
n (n_0)	Number density (stagnation)
$n_{t,lim}$	Min. thruster number density limit
P	Power
R	Specific gas constant
R_E	Equatorial Earth radius
R_u	Universal gas constant
Re_l	Reynolds number
S	Molecular speed ratio
SA	Solar activity
T	Temperature
t	Array thickness or Time
T_{max}	Maximum wall temperature
T_r	Reflected particle temperature
T_w	Wall temperature
u	Flow velocity
u_e	Exhaust velocity
∞	Subscript for onset flow
a	Subscript for array
b	Subscript for flow into intake
c	Subscript for back-scattered intake flow
i	Subscript for intake
n	Subscript for collector
s	Subscript for side
t	Subscript for thruster
$\bar{}$	Superscript for mean orbital element
ABEP	Air-breathing electric propulsion
DSMC	Direct Simulation Monte-Carlo
GMAT	General Mission Analysis Tool
RAAN	Right ascension of the ascending node
SSO	Sun-synchronous orbit
VLEO	Very low Earth orbit

A more general system-level analysis was then presented by Di Cara et al. [5] at ESA in 2007, which provided an initial estimate of the altitude limits. An approximate lower limit of 180–200 km was found and an upper limit of around 250 km was obtained from considering the propellant mass needed for conventional electric thrusters to provide a given operational lifetime. The analysis concluded that the small conventional propellant mass needed meant that an air-breathing system was not worthwhile for orbits above 250 km. The study identified the important considerations of solar activity on atmospheric properties and the likelihood of only thrusting for fractions of the orbital period due to eclipses in all other than a dawn–dusk Sun-synchronous orbit (SSO).

An analysis of ABEP was presented by Romano et al. [6,7] and Romano [8] at the University of Stuttgart from 2015. This study presented the variation of atmospheric properties with solar activity and calculated the drag for specific sizes of spacecraft to obtain an estimate of the thrust required. A method for finding drag in free-molecular flow was presented, however a simple constant drag coefficient of 2.2 was preferred to reduce uncertainty. An intake analysis using the DSMC method was done to show agreement with results of the JAXA study and a semi-analytical method of intake design was presented, before further work on developing an inductive plasma thruster.

Studies were performed by members of the AETHER project, first by Barral et al. [9] and then Andreussi et al. [10,11] and Ferrato et al. [12] from 2015, led by Sitael. Similarly to JAXA, an intake design

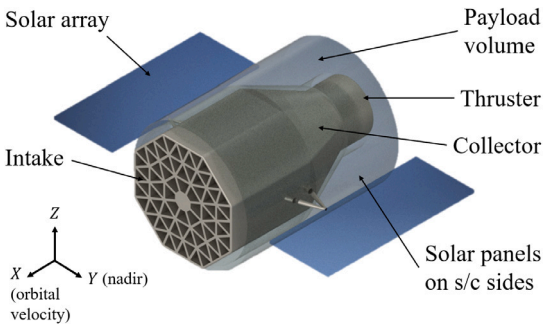

Fig. 1. Simplified spacecraft model.

analysis focused on the balance between thruster mass flow and density using DSMC simulations. A requirement for minimum exhaust velocity with altitude was found based on compensating intake pressure drag. Further work was conducted in testing a complete system prototype, featuring a Hall thruster for creating atmospheric conditions representative of VLEO, an intake, an ionisation stage of proprietary design and an acceleration stage for air based on a Hall thruster. In 2019, the intake performance was studied in more detail by Parodi et al. [13] at the Von Karman institute. This provided a useful summary of the effect of atmospheric conditions on intake performance and presented an optimisation method for the intake design. The latest work by Ferrato et al. [12] focused on mission scenarios and a system analysis to optimise the air-breathing thruster for a range of altitudes, including intake performance and spacecraft drag in the model. A propagation of the spacecraft orbit with time was presented for a particular thruster design, using a simple control law instructing thruster operation when the semi-major axis fell below the target value.

A review of the existing ABEP literature highlights a focus on the development and optimisation of particular thruster designs. The first part of this study addresses the lack of an analysis which links the feasible operating altitude to the thruster performance and spacecraft parameters, for a generic electric thruster and spacecraft configuration. This drag-compensation analysis additionally considers the key drag contribution of lateral spacecraft surfaces, which has been neglected in the majority of previous studies. As a result, the flight envelope of a generic ABEP spacecraft can be identified. The second part of this study investigates the orbital variation with time of an air-breathing spacecraft to determine the feasibility of a long-term, stable altitude profile. This differs from the majority of existing literature where a circular orbit is assumed, however this is not naturally possible in VLEO due to the non-sphericity of the Earth's gravity. A key divergent altitude behaviour is identified, which is addressed through the use of a thruster control law that provides robustness against time-varying atmospheric properties.

2. Dynamics and spacecraft model

The implemented system-level approach models the atmospheric properties, drag produced by different spacecraft surfaces and performance of a passive intake feeding air to the electric thruster. The requirements of the air intake, electric propulsion system and solar arrays, which constitute the main components of the spacecraft platform, are interconnected. In this study, analytical solutions complemented by data from literature are preferred over more complex simulation approaches, aiming at a general assessment on the conditions and key parameters needed to enable feasible air-breathing missions at varying altitudes.

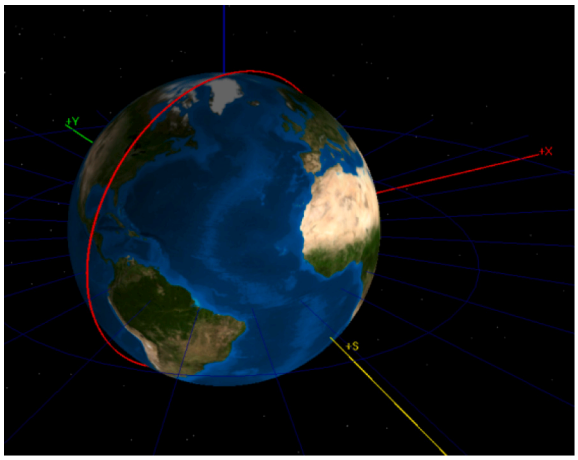

Fig. 2. Dawn-dusk SSO with mean semi-major axis altitude of 200 km shown in January 2000 using International Celestial Reference Frame. Blue vertical and +S yellow lines correspond to Z-axis and Sun vector respectively. (For interpretation of the references to colour in this figure legend, the reader is referred to the web version of this article.)

2.1. Spacecraft overview

The ABEP principle is summarised in reference to the generic model shown in Fig. 1. The onset airflow passes through the intake and collector to the thruster. The air is decelerated before the entrance to the thruster to achieve compression to a higher density, and is then ionised and accelerated to produce thrust. The solar arrays are simply assumed to produce electrical power for the thruster, with both intake and solar array area needing to increase for a propulsion system producing a higher thrust.

The nominal orientation of the satellite is assumed to be with the intake perpendicular to the onset flow and the solar arrays parallel to the flow vector, as shown in Fig. 1. The ratio of intake diameter to length of the satellite body is defined as the spacecraft aspect ratio AR_s, which was estimated in the $AR_s \approx 1$ order of magnitude from previous literature [3,6]. The orientation of the intake would be maintained perpendicular to the onset flow to maximise intake performance. A parallel solar array orientation to the flow is the preferred design for minimum drag. It is a realistic configuration for a SSO with a dawn–dusk terminator as it positions the array surface normal to the Sun vector for optimal power generation. Such an orbit is visualised in Fig. 2. To clarify, the orbital plane is closest to the perpendicular condition with the Sun vector in the Spring and Autumn seasons, whereas there is an appreciable offset between the normal to the orbital plane and the Sun vector during the Winter and Summer seasons, as can be seen in Fig. 2. This orientation and orbit type was used by the ESA GOCE spacecraft [14] so was seen as a useful starting point for this study, however both the orientation of the body and arrays can be varied in the model to simulate different missions and orbits.

2.2. Onset flow velocity

The velocity of the onset flow u_∞ is assumed equal to the spacecraft orbital speed. The ∞ subscript indicates a value for the onset flow (or freestream). The velocity depends on the altitude of the orbit as per the Vis-Viva equation derived from orbital energy conservation. The first part of this study assumes a circular orbit and the Earth's rotation is neglected, leading to:

$$u_\infty = \sqrt{\frac{\mu_E}{R_E + H}} \tag{1}$$

where $\mu_E = 3.986 \times 10^{14}$ m^3/s^2 is the standard gravitational parameter of Earth, $R_E = 6.378 \times 10^6$ m is the equatorial Earth radius and H is the orbital altitude.

The onset flow velocity of air entering the intake is affected by lateral components of the air's motion in the upper atmosphere and the alignment between the intake axis and the direction of flight, giving an effective yaw angle ψ. The component of ψ from alignment of the satellite is achieved by the attitude control system. The lateral component of the onset flow, caused by air currents and the corotation of the atmosphere, has a larger effect on ψ and has been analysed in the literature using a model for horizontal atmospheric winds [13]. It was found that a maximum of $\psi = 4°$ could be expected for a SSO in the low altitude range, with smaller angles for lower inclination orbits. Parodi et al. [13] found that the performance of the intake (in compression ratio and collection efficiency) was reduced by around 10% for a realistic worst-case $\psi = 5°$ using a DSMC simulation. The assumption used in this study of negligible atmospheric contribution to ψ is therefore seen as a reasonable simplification, given that corrections to the intake performance can be implemented based on this previous literature.

2.3. Atmospheric model

The NRLMSISE-00 model was chosen to find the variation of atmospheric properties with altitude. It is one of two atmospheric models, alongside JB2008, that are recommended by the ESA Space Environment Standard [15]. The models provide data on air temperature, total density and density of the air's constituent gases. NRLMSISE-00 is considered more accurate for individual gas species and the JB2008 model more accurate for total mass density, however previous studies in the literature have found little difference between the models [13]. The model produces data for altitudes up to 1000 km of equilibrium air temperature T_∞, total mass density ρ_∞ and number density n_∞ for each gas species. The effect of altitude on gas number density and composition is shown in Fig. 3. Molecular nitrogen N_2 and oxygen are the most prevalent gas species. It should be noted that atomic oxygen O becomes more common than O_2 at ~110 km and the most numerous species after ~170 km.

The NRLMSISE-00 model includes the effect of solar activity on atmospheric properties, in the form of an input for the 10.7 cm solar radio flux index $F10.7$ and the magnetic Ap index. $F10.7$ is a measure of the solar radiation in the wavelengths that cause atmospheric ionisation and Ap represents the variation in the daily average of the Earth's magnetic field. Typical values for both indexes were analysed from the NOAA records database [16] and previous literature [7]. The nominal average values were chosen as $F10.7 = 140$, $Ap = 15$, minimum values as $F10.7 = 70$, $Ap = 8$ and maximum values as $F10.7 = 250$, $Ap = 100$.

The atmospheric properties vary appreciably with solar activity, geographic location and time of year. An analysis was done at a representative altitude of 180 km relative to R_E to find the trends in air density, temperature and composition over the three sets of $F10.7$ and Ap values, a range of latitudes and longitudes covering the Earth, and two seasonal extremes of January and July. The variation factor of each atmospheric property is defined as max/min and these values are shown in Table 1, along with the property range and a summary of seasonal trends. The max. combined variation factors combine the effects of solar activity, location and time of year to give an idea of the largest expected change encountered by an ABEP spacecraft with an operating life in the order of an 11-year solar cycle.

Both density and temperature increase with $F10.7$ and Ap. While there is a trend for lower densities at northern latitudes in January and at southern latitudes in July, the density is changeable across most of the remaining latitudes and longitudes. The variation in onset density, approximately between 7×10^{15}–3×10^{16} m^{-3}, is the most significant for an air-breathing spacecraft as it is directly proportional to drag. This shows that spacecraft drag, and to a lesser extent heating, can vary over a single orbit as well as the spacecraft lifetime.

For a fixed 180 km altitude, the major species in the air are N_2 and O. The air's composition is particularly strongly affected by variations in latitude, more so than solar activity, which results in broad ranges of 0.34–0.85 for the N_2 fraction and 0.09–0.63 for the O fraction. Even for a fixed operating altitude, it is important that an air-breathing thruster is effective at ionising and accelerating multiple gas species. The effect of solar activity on the results obtained from the model is considered as part of this study. In order to account for the short-term variability of the atmospheric properties and simulate a realistic scenario, the performance of an ABEP spacecraft is analysed over the course of several propagated orbits using a given thruster operating envelope.

The gas properties of air in this model are calculated according to standard ideal, calorically-perfect gas theory. A value of specific heat ratio $\gamma_h = 5/3$ is assumed for upper atmospheric conditions [4] and its temperature dependence is neglected due to the typically small effect [17, p. 57]. The $\gamma_h = 5/3$ value typical for monatomic gases is used to model a mixture containing both monatomic and diatomic species, rather than the diatomic value of $\gamma_h = 7/5$. This is because excitation of the two extra rotational degrees of freedom typically present in a diatomic gas is negligible given the low collision frequency of particles in VLEO (see Section 3).

3. Flow regimes and drag calculations

Three different types of flow are considered at the VLEO altitudes of interest, presented here in order of ascending altitude: continuous, transitional and free-molecular flow (FMF). The Knudsen number Kn is used to find the altitude range at which flow can be modelled to transition from the continuous to free-molecular regime. It is a ratio of the mean free path λ to the characteristic length of the body, here the satellite length L. Flow is assumed as continuous for $Kn \ll 1$, with particles colliding many times over the distance of the body. It is assumed as free-molecular for $Kn \gg 1$, since particles reflected from the body travel far before colliding with others, and the body can be approximated as having no influence on the collective onset flow [18]. Kn is found as:

$$Kn = \frac{\lambda}{L} = \frac{m_\infty}{\sqrt{2}\pi d^2 \rho_\infty L} \tag{2}$$

where d is the effective molecular diameter of the air and m_∞ is the average air molecular mass (in kg). A value of $d = 4 \times 10^{-10}$ m is used as per VLEO flow models in the literature [19, p. 22] [13] and $L = 1$ m is taken as a reasonable approximation.

The Kn values used to mark the upper and lower altitude limits of the continuous and free-molecular regimes are the most common in literature [18,20], and are shown in Table 2. From Kn, the altitudes of the flow regimes allow a calculation of the drag profile over the full altitude range.

3.1. Continuous flow drag

In the continuous flow regime, the air is assumed to act as a fluid in which particles display a collective motion. This results in macroscopic fluid behaviour, such as the formation of a boundary layer at the interface with the spacecraft body. The Reynolds number Re_l characterises the fluid in this regime as per Eq. (3). Re_l was found to be approximately 10^3–10^4 for the lower range of the altitudes considered (≈80–85 km) where the flow is still continuous.

$$Re_l = \frac{\rho_\infty u_\infty L}{\mu} \tag{3}$$

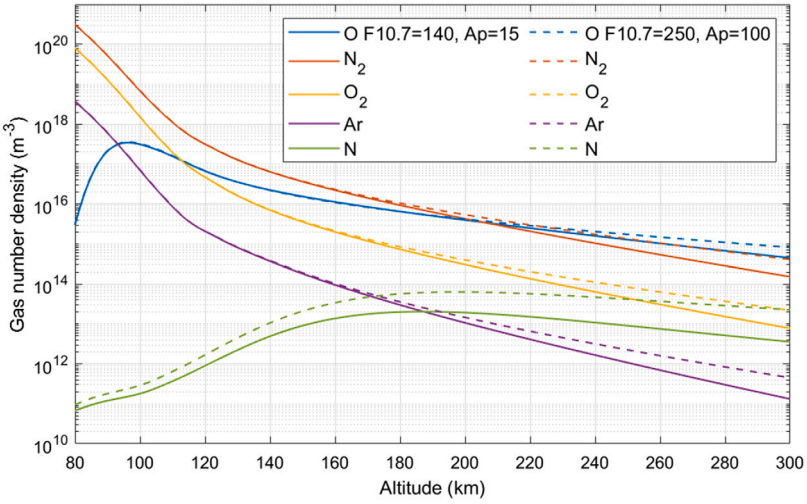

Fig. 3. Gas number density with altitude for nominal and maximum solar activity. Data is averaged over dawn–dusk SSO latitudes/longitudes, times of day and days of year.

Table 1
Variation factor of atmospheric properties at 180 km relative to R_E with solar activity, location and seasonal trends. N and S correspond to northern and southern respectively. 'Factor' refers to max/min values over full range of property in question.

	n_∞	T_∞	O fraction	N_2 fraction
Solar activity factor	2.2	1.6	2.3	1.1
Geo-location factor	2.6	1.6	6.6	2.3
Max. combined factor	4.5	2.4	7.0	2.5
Max. combined range	7.0×10^{15} – 3.2×10^{16} m^{-3}	555–1333 K	0.09–0.63	0.34–0.85
January	Low at N polar lats.	High at S polar lats.	High at N lats.	High at S lats.
July	High at S polar lats.	High at N polar lats.	High at S lats.	High at N lats.

Table 2
Definition of flow regimes.

Flow regime	Kn	Altitude (km)
Continuous	<0.01	Below ~85
Transition	0.01–10	~85–130
Free-molecular	>10	Above ~130

where μ is the dynamic viscosity, found using the Sutherland formula [21] in which μ is a function of the air temperature. The relation used is:

$$\mu = \frac{1.458\times10^{-6}\ \sqrt{T_\infty}}{1+110.4\ T_\infty^{-1}} \tag{4}$$

The drag in the continuous regime is calculated from a simplified model of the flow behaviour, approximating the satellite surfaces as a combination of two flat plate configurations: perpendicular and parallel to the onset flow.

The perpendicular flat plate is dominated by pressure drag and a constant pressure drag coefficient C_{Dp}^{cont} is used in the continuous flow regime, which is the analytical solution for a perpendicular flat plate. This value is independent of Re_l [22] and is commonly assumed for hypersonic flow [23, p. 694]:

$$C_{Dp}^{cont} = \text{const.} = 2 \tag{5}$$

The parallel flat plate is dominated by viscous (or skin friction) drag. The friction drag coefficient C_{Df}^{cont} was found using the Blasius laminar flow solution for a parallel flat plate, as per Eq. (6). This method avoids introducing uncertainty, with the laminar approximation being valid as $Re_l \ll 10^5$–10^6 where transition to turbulent flow begins [22]:

$$C_{Df}^{cont} = \frac{1.328}{\sqrt{Re_l}} \tag{6}$$

The total continuous drag coefficient is then found from the addition of C_{Dp}^{cont} and C_{Df}^{cont}, depending on the angle α_j of each surface j to the onset flow. Eqs. (7)–(9) introduce $C_{D,i}^{cont}$ for the intake, $C_{D,s}^{cont}$ for the spacecraft sides and $C_{D,a}^{cont}$ for the solar arrays. Assuming the intake is approximately perpendicular to the flow, negligible attachment of the flow along the sides of the spacecraft is assumed. The viscous drag along the spacecraft sides can therefore be ignored in the continuous regime. This assumption is based on typical laminar flow visualisation for approximately perpendicular flat plates at the Re_l range in question [24].

$$C_{D,i}^{cont} = C_{Dp}^{cont}\sin(\alpha_i) + C_{Df}^{cont}\cos(\alpha_i) \tag{7}$$

$$C_{D,s}^{cont} = 0 \tag{8}$$

$$C_{D,a}^{cont} = C_{Dp}^{cont}\sin(\alpha_a) + C_{Df}^{cont}\cos(\alpha_a) \tag{9}$$

The angles ψ, θ and ϕ represent the orientation of the spacecraft body to u_∞, defined here as yaw, pitch and roll respectively, as shown in Fig. 4. The array pitch θ_a is independent of the body value and the intake pitch $\theta_i = \theta + \pi/2$. The resultant angle from the sum of the yaw, pitch and roll rotations between each surface j and the onset flow is α_j, calculated from the scalar product of the surface normal and u_∞. As shown in Fig. 4, α_t is the resultant angle between the spacecraft central axis and the onset flow.

3.2. Free-molecular flow drag

In the free-molecular flow regime, the air is assumed to act as individual particles and forces imparted on the body are calculated from the momentum transfer of particle collisions. Based on the process of Schaaf and Chambre [18], Bird [19] and Shen [20], the pressure and shear stresses are calculated from the difference between incident and reflected momentum flux of particles, and integrated to give a drag coefficient. The nature of particle collisions with the surface is simplified as either diffuse or specular. Diffuse reflections are entirely

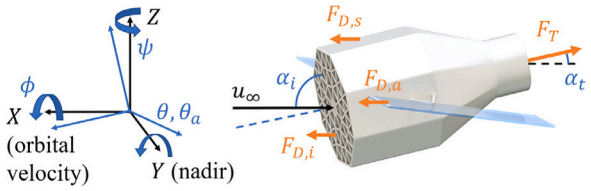

Fig. 4. Diagram of satellite orientation and forces, with α_t shown for the spacecraft thrust vector and α_i for the intake.

responsible for skin friction (tangential) drag in free-molecular flow. The average proportion of diffuse reflections is σ, and so the fraction of specular reflections ϵ is simply $\epsilon = 1 - \sigma$.

The molecular speed ratio S_∞ is defined as per Eq. (10), which is equivalent to the Mach number in continuous flow [20].

$$S_\infty = \frac{u_\infty}{\sqrt{2RT_\infty}} = u_\infty \sqrt{\frac{M_\infty}{2R_u T_\infty}} \tag{10}$$

where M_∞ is the average molar mass (in kg/mol) and R_u is the universal gas constant. This shows that S_∞ is proportional to the square root of the average molar mass of the air for a given value of T_∞. As shown in the following sections, the free-molecular drag coefficient is broadly inversely proportional to S_∞ [18, p. 20–22], and therefore similarly to $\sqrt{M_\infty}$ if the effect of temperature is ignored.

The drag coefficient C_D^{fmf} for a flat plate in molecular flow is obtained analytically in [18–20]. The formulation presented here includes terms from both specular and diffuse reflections, and therefore depends on the angle of the flat plate to the onset flow α. As in the continuous regime, the drag coefficient is split into three values: $C_{D,i}^{fmf}$ for the intake, $C_{D,s}^{fmf}$ for the spacecraft sides and $C_{D,a}^{fmf}$ for the solar arrays. The drag coefficients for the intake and arrays are calculated as per Eq. (11)–(12). A distinction is made between the number of surface sides exposed to the onset flow; one side for the intake and both sides for the arrays. The first term in Eqs. (11) and (12) corresponds to the skin-friction drag, so depends on the number of exposed sides and is therefore doubled for the arrays. It should be noted that neglecting the drag contribution from the frontal edge area of the solar arrays is a simplification. For reference, an array length to thickness ratio $c/t \sim 200$ is required to decrease the frontal array edge area drag contribution to 10% of that resulting from the area aligned nominally parallel to the flow, assuming C_D values of the same order as those presented in Section 3.3 later. Concerning the intake, a proportion of the collected flow does not pass through to the intake exit but is instead scattered back out of the inlet (see Section 4.1); for this fraction of the onset flow, the intake acts as an effective flat surface, angled approximately perpendicular to the onset flow vector to maximise flow collection. The final intake drag term is multiplied by a factor $(1-\eta_c)$ representing the fraction of flow which is back-scattered (see Section 5), which is the same approach used in [11,25].

$$C_{D,i}^{fmf} = \frac{\left[1-\epsilon\cos(2\alpha_i)\right]}{\sqrt{\pi}S_\infty} e^{-S_\infty^2 \sin^2(\alpha_i)} + \frac{\sin(\alpha_i)}{S_\infty^2} \cdot \left[1 + 2S_\infty^2 + \epsilon\left(1 - 2S_\infty^2 \cos(2\alpha_i)\right)\right] \cdot erf\left(S_\infty \sin(\alpha_i)\right) + \frac{(1-\epsilon)}{S_\infty}\sqrt{\pi}\sin^2(\alpha_i)\sqrt{\frac{T_r}{T_\infty}} \tag{11}$$

$$C_{D,a}^{fmf} = \frac{2\left[1-\epsilon\cos(2\alpha_a)\right]}{\sqrt{\pi}S_\infty} e^{-S_\infty^2 \sin^2(\alpha_a)} + \ldots \tag{12}$$

where *erf* is the error function and T_r is the temperature of the reflected particles. $C_{D,s}^{fmf}$ is calculated by dividing the cylindrical side surface into strips and summing the drag coefficient obtained for each. This is shown in Eq. (13), where k is the number of strips. The formula used for each strip is the same as Eq. (11) for the intake. The drag contribution of strips shaded from the onset flow by the intake is neglected.

$$C_{D,s}^{fmf} = \sum_1^k \frac{1}{k} C_{D,k}^{fmf}(\alpha_k) \tag{13}$$

- It is assumed that particles colliding with the surface are fully accommodated and so reflected with a Maxwellian distribution that corresponds to the surface wall temperature [20, p. 165]. Therefore, $T_r \approx T_w$.
- The value of σ has a large influence on the drag coefficient, particularly as skin-friction drag does not occur with entirely specular reflection. It is commonly assumed that reflections are almost fully diffuse ($\sigma \to 1$) in orbital conditions [19, p. 170][18, p. 11][13], so $\sigma = 0.9$ is used here.

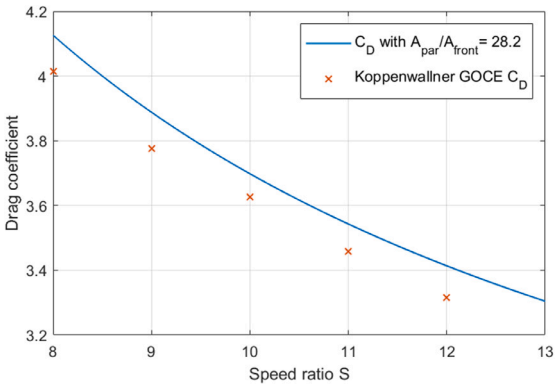

Fig. 5. Comparison of body free-molecular C_D with $A_{par}/A_{front} = 28.2$ [26].

The calculation of drag in free-molecular flow, the regime for the majority of the altitude range considered, was verified through comparison to results in the literature. Koppenwallner [26] modelled the drag coefficient of the GOCE spacecraft using DSMC simulations. A ratio of the areas parallel and perpendicular to the flow was defined as A_{par}/A_{front}, which here represents the spacecraft side area over the intake area A_s/A_i, with this value equal to 28.2 for GOCE. The C_D value was taken with reference to GOCE's front surface (here the intake) so the following expression allowed comparison:

$$C_{D,total}^{fmf} = C_{D,i}^{fmf} + C_{D,s}^{fmf} \frac{A_{par}}{A_{front}} \tag{14}$$

A comparison of the results for $A_{par}/A_{front} = 28.2$ plotted against speed ratio is shown in Fig. 5, which indicates good agreement with a maximum difference of 3%. $T_w/T_\infty = 0.3$ and $\sigma = 1$ were assumed to match Koppenwallner [26].

The analytical drag coefficient calculation used here was also compared to a common reference test case for DSMC models of a parallel flat plate in rarefied, hypersonic flow. This was presented by Padilla [27]. The model inputs were plate dimensions of 5 mm width and 100 mm length, $u_\infty = 1503$ m/s, molecular nitrogen flow with $n = 3.72\times10^{20}$ m^{-3} and $d = 4.2\times10^{-10}$ m, $T_\infty = 13.3$ K and $T_w = 290$ K. The DSMC models assumed full diffuse reflection ($\sigma = 1$). This resulted in a speed ratio $S_\infty = 16.9$ and Knudsen number $Kn = 0.035$ for $L = 100$ mm.

Since a parallel flat plate was modelled, the skin friction drag coefficient was analysed, and this comparison is shown in Fig. 6. There is good agreement between the constant analytical free-molecular solution and the averaged DSMC results, with a 6% error. However, the DSMC model requires making the same assumption about the ratio of diffuse to specular reflections. It should also be noted that the low Knudsen number means this flow is much closer to the continuous approximation than the $Kn > 10$ free-molecular requirement. It is therefore expected that the analytical drag solution over-estimates the skin-friction coefficient compared to its continuous value (see Fig. 8).

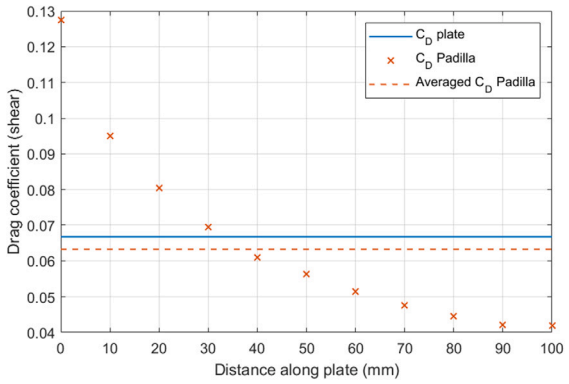

Fig. 6. Comparison of flat plate C_D to DSMC reference using addition of strips for $Kn = 0.035$ [27].

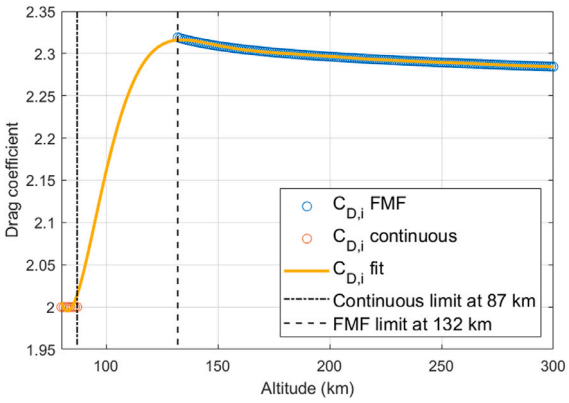

Fig. 7. Variation of intake $C_{D,i}$ with altitude.

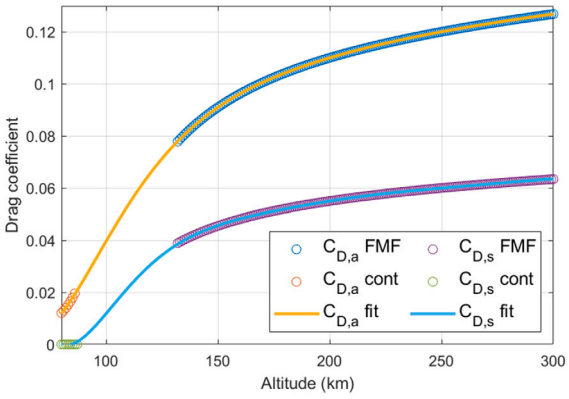

Fig. 8. Variation of array $C_{D,a}$ and spacecraft side $C_{D,s}$ with altitude.

3.3. Transitional flow drag

The transitional regime describes flow between fully continuous and fully free-molecular behaviour, so both collective fluid and particle motions are present. To avoid further uncertainty in attempting to model the transitional regime, this analysis uses an interpolation between the continuous and free-molecular C_D values. A polynomial of order 9–12 was found to give a least-squares fit that reasonably retained the constant $C_{D,i}^{cont}$ and $C_{D,s}$ values. Combining the three flow regimes, the variation of drag coefficients $C_{D,i}$, $C_{D,s}$ and $C_{D,a}$ with altitude is shown in Figs. 7 and 8.

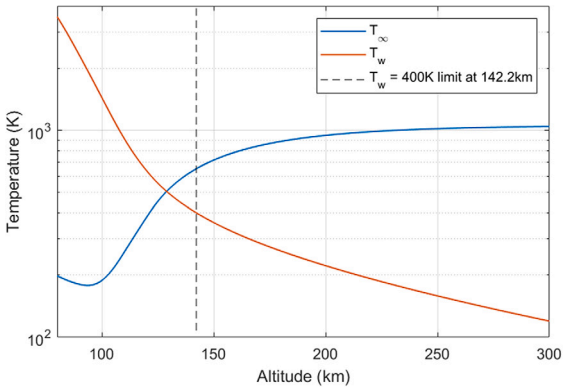

Fig. 9. Variation of temperature with altitude. Data is averaged over dawn–dusk SSO latitudes/longitudes, times of day and days of year.

3.4. Spacecraft heating

A limit on the minimum operational altitude of an air-breathing satellite is the heating of the spacecraft walls from flying through denser layers of the atmosphere. The wall temperature T_w is therefore calculated, to identify altitudes where heating would lead to temperatures above the allowable limit T_{max}. This is done using a simplified version of the heat transfer energy equation for a 1D, steady-state scenario following the procedure of Fujita [4]. The highest wall temperature is found to occur at the intake surface, for which the energy transferred by the onset flow through convection is equated to the net heat energy radiated. The relation is shown in Eq. (15), with both terms normalised for area. This is a worst-case scenario for heating from the onset flow as it assumes stagnation conditions with all particles led adiabatically to rest at the front surface and no conduction through the wall.

$$\rho_\infty u_\infty h_0 = \rho_\infty u_\infty \left(\frac{u_\infty^2}{2} + h\right) = \epsilon_r \sigma_{SB} T_w^4$$
$$T_w = \left(\frac{\rho_\infty u_\infty \left(u_\infty^2/2 + h\right)}{\epsilon_r \sigma_{SB}}\right)^{1/4} \tag{15}$$

where h is the specific enthalpy in J/kg (h_0 is the stagnation value), ϵ_r is the reflectivity of the satellite frontal area assumed equal to 0.5 [4] and $\sigma_{SB} = 5.67 \times 10^{-8}$ W/m^2 K^4 is the Stefan–Boltzmann constant. This simplification shows close agreement to the temperature variation with altitude presented by Bird [19, p.169], calculated from free-molecular theory. The variation of T_∞ and T_w is shown in Fig. 9. The ratio T_w/T_∞ is used to calculate free-molecular C_D and varies with altitude between 0.1–0.9. Setting T_{max} = 400 K produces an altitude limit of 142 km, compared to the more general 120 km heating limit identified by Young et al. [28]. Given the drag-compensation solution results in Section 5, the lower limit of the feasible altitude range is not found to be set by spacecraft heating.

It is possible to include terms for solar radiation flux, Earth albedo and internal power dissipation in Eq. (15). However, these have been neglected for this simple model as the intake surface is shielded from the Sun vector in the nominal dawn–dusk SSO configuration and the majority of internal power dissipation will not occur via the intake surface. Flow heating of the spacecraft sides is found to be less significant than solar radiation and internal power dissipation due to a lower particle flux density than the intake. This results in a lower maximum temperature for the spacecraft sides of around 320K, which is mainly constant with altitude, and so the T_w limit is based on the intake.

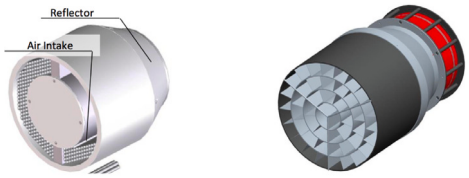

(a) JAXA, from [7]. (b) Sitael, from [11].

Fig. 10. Intake concepts.

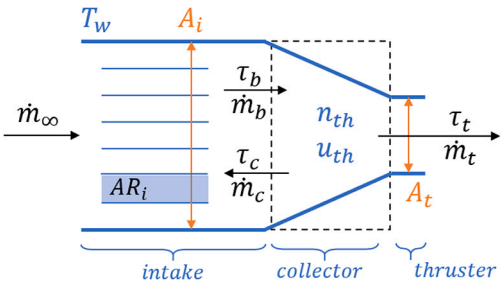

Fig. 11. Diagram of intake flows.

4. Sub-system models

4.1. Intake design

Several intake designs were considered in the literature. The two most analysed intake designs are those of JAXA [3,4,6] and more recently Sitael [9,13]. The JAXA proposal considers the intake as an outer ring around a smaller cylinder which forms the body of the satellite, as shown in Fig. 10(a). The Sitael concept assumes a cylindrical intake covering the full satellite frontal area, as shown in Fig. 10(b). The aspect ratio of the intake duct AR_i compares the intake length to the diameter. The division of the frontal area into smaller diameter cylindrical sections in the Sitael intake results in an effective $AR_i = 6$. The intakes differ in drag generation, as the inner cylinder of the JAXA intake provides payload volume and forms a solid boundary to the flow.

This study assumes an intake of the form of the Sitael concept, where the intake forms the full frontal area of the satellite. This concept is considered more widely-applicable due to its simplicity. The intake for the air-breathing concept has two principal functions:

- To collect the mass flow of the incoming air into the thruster, for ionisation and acceleration. The mass flow rate at the thruster $\dot{m}_t$ needs to be sufficiently high for thruster operation. This results in the first intake performance metric: **collection efficiency** η_c. This represents the ratio of mass flow rates between the onset flow at the intake entrance $\dot{m}_\infty$ and the thruster at the intake exit, as per Eq. (16). A_i is the intake area.

$$\eta_c = \frac{\dot{m}_t}{\dot{m}_\infty} = \frac{\dot{m}_t}{\rho_\infty A_i u_\infty} \quad \rightarrow \quad \dot{m}_t = \eta_c \rho_\infty A_i u_\infty \tag{16}$$

- To increase the density of air by compressing the onset flow n_∞ to a higher value at the thruster n_t. A sufficiently high density is required to create plasma properties inside the thruster that allow propellant acceleration. This results in the second intake performance metric: **compression ratio** β. This represents the density ratio between the intake entrance and exit, and is found for both the static density (β) and the stagnation density (β_0):

$$\beta = \frac{n_t}{n_\infty} = \frac{\rho_t}{\rho_\infty} \qquad \beta_0 = \frac{n_{0,t}}{n_\infty} = \frac{\rho_{0,t}}{\rho_\infty} \tag{17}$$

The global collection efficiency is based on a combination of transmittance values. Transmittance τ is defined here as the fraction of particles that travel through a section compared to the number of particles incident onto the start of the section, as a portion of particles are back-scattered and do not reach the section exit [6]. The total intake can be simplified in 1D as shown in Fig. 11, with τ_b for the fraction of flow crossing the intake and reaching the collector, τ_c for flow back-scattered out of the intake and τ_t for flow into the thruster. The accompanying mass flow rates $\dot{m}$ are shown.

Applying continuity to the collector and noting that $\dot{m}_b = \dot{m}_\infty \tau_b$:

$$\dot{m}_b = \dot{m}_\infty \tau_b = \dot{m}_c + \dot{m}_t \tag{18}$$

$$\frac{\dot{m}_\infty}{\dot{m}_t}\tau_b = \frac{\tau_b}{\eta_c} = \frac{\dot{m}_c + \dot{m}_t}{\dot{m}_t} = \frac{\left(A_i\tau_c + A_t\tau_t\right)}{A_t\tau_t} \tag{19}$$

$$\eta_c = \tau_b A_t \frac{\tau_t}{A_i\tau_c + A_t\tau_t} \tag{20}$$

where A_t is the thruster area. Returning to the continuity Eq. (18), since $\dot{m} = \rho A u = mnAu$ and m is constant:

$$n_\infty A_i u_\infty \tau_b = n_n u_{th}\left(A_i\tau_c + A_t\tau_t\right) \tag{21}$$

where n_n is the number density of the air in the collector and $u_{th} = \sqrt{k_B T_n}/\sqrt{2\pi m_n}$ is the effective flux-derived velocity in a single direction under the assumption of a Maxwellian velocity distribution. This is based on the thermal mass flux definition of free-molecular flow applied to the inside of the collector, as per [19, p. 151]. It can be assumed that the air at the collector has lost all its axial velocity, either through direct collisions with the conical collector sides or collisions with other particles, and is fully thermalised with a Maxwellian velocity distribution. The compression ratio can therefore be expressed as:

$$\beta = \frac{n_t}{n_\infty} \approx \frac{n_n}{n_\infty} = \frac{\tau_b A_i u_\infty}{u_{th}} \frac{1}{A_i\tau_c + A_t\tau_t} \tag{22}$$

As a rough approximation, this formulation shows that $\eta_c \propto \tau_t$ whereas $\beta \propto 1/\tau_t$, so it is not possible to simultaneously maximise both collection efficiency and compression ratio for a given τ_b [3]. This can be intuitively understood since a high η_c requires a large flow velocity, reducing the residency time and so density of particles in the collector. The two intake performance indices are crucial in defining the operating altitude of an air-breathing satellite. The lower altitude limit is set by an increasing specific impulse requirement, however this is relaxed by increasing η_c. The upper altitude limit is set by the drop-off in n_t, however this is relaxed with a high β. The transmittance values that determine η_c and β are influenced by the intake design through changes of AR_i and the area ratio A_t/A_i.

4.2. Collection efficiency η_c

The calculation of transmittance values requires simulation of the free-molecular flow for a given intake geometry, which is done using DSMC methods. This is beyond the scope of this study but has been done in the literature [3,6,9,13]. Typical η_c values in the range of 0.3–0.5 are predicted by these studies, therefore this is the range of collection efficiency considered in this analysis.

4.3. Compression ratio β

The stagnation compression ratio β_0 represents the maximum achievable compression as the air at the thruster is assumed to have zero dynamic component. β_0 can be found analytically but a correction is needed to account for the lower, realistic compression value of β achievable in the intake. β_0 is calculated as per Eq. (23) which follows the procedure of Fujita [4], derived from stagnation conditions of isentropic flow:

$$\beta_0 = \left(1 + \frac{u_\infty^2}{2h}\right)^{1/\gamma_h - 1} \tag{23}$$

Table 3
Comparison of β approximation to literature values [13].

Parameters								
AR_i	T_w (K)	T_∞ (K)	u_∞ (m/s)	γ_h	N_2 fraction	O fraction	η_c of N_2 (from [13])	η_c of O (from [13])
6	300	800	7800	5/3	0.55	0.45	0.2901	0.2521
Results comparison								
Parodi simulation data:					average $\beta = 92.6$			
Interpolation method of Eq. (24):					average $\beta = 99.9$			

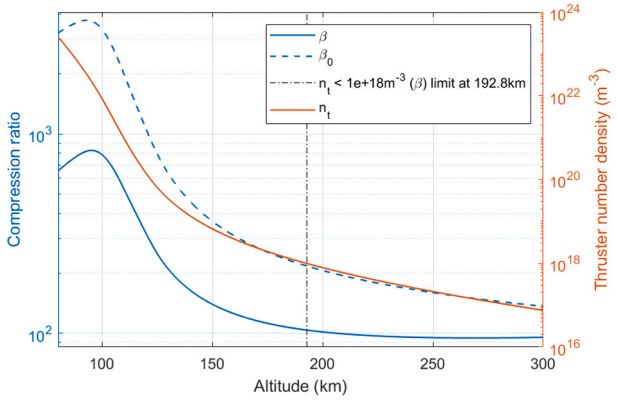

Fig. 12. Variation of compression ratio and number density at thruster with altitude, for $\eta_c = 0.35$ and $AR_i = 14$. Data is averaged over dawn–dusk SSO latitudes/longitudes, times of day and days of year.

A more realistic value for the compression ratio is obtained by accounting for the effect of the wall temperature T_w, the intake aspect ratio AR_i and the collection efficiency η_c, which is shown in Eq. (24). This follows the interpolation developed by Fujita [4] from DSMC simulations, in order to provide a simple analytical method of estimating β. The DSMC simulations used in the cited study were performed for a representative 180 km altitude with a gas species composition of 0.51 N_2, 0.46 O and 0.03 O_2, which matches well with the composition ranges modelled here (see Table 1). The normalisation of the approximation to β_0 improves its applicability to a degree of variation in composition.

$$\beta = 0.87\beta_0 \left(0.244 + 0.33\ln(AR_i)\right) \cdot \left(\frac{189}{T_w + 33} + 0.435\right) \cdot \left(1 - 1.625\eta_c\right) \tag{24}$$

The compression ratios and resulting densities are plotted in Fig. 12. This allows an upper altitude limit to be set for the operating region of an air-breathing satellite, when the atmospheric density becomes too low for the compression to achieve the minimum required n_t. The limit is also shown in Fig. 12 for a minimum $n_{t,lim} = 10^{18}$ m^{-3}, which is based on the value used in the literature for an ion engine [4] and Hall thruster [10] concept using an ionisation stage upstream of the thruster. The adoption and optimisation of a dedicated ionisation stage, which is common for gridded-ion thrusters, could have a fundamental role in lowering the density limit for thruster operation and allowing an increase of the maximum operating altitude.

The compression ratio results were compared to those obtained by Parodi et al. [13] from 3D DSMC simulations in order to check the reliability of the interpolation method, and this is shown in Table 3. The study modelled an intake with channels of $AR_i = 6$ and conditions representative of a 160 km altitude, obtaining β values for N_2 and O as these species are the major components of air at that altitude. Averaging the results based on proportions of 55% N_2 and 45% O gives $\beta = 92.6$ for Parodi et al. [13], compared to $\beta = 99.9$ for the method of Eq. (24). The results are in a similar range with a discrepancy of 8%, suggesting that the interpolation method provides a reasonable estimate of β.

4.4. Solar arrays

The satellite solar arrays are modelled in this study to represent the increased solar array area required for generating a higher thrust, due to the corresponding thruster power. A larger array area would result in an increased shear drag, so it is predicted that this may place a limit on the operating altitude. The thruster performance is related to the power P_t via the total thruster efficiency η_T:

$$P_t = \frac{F_T u_e}{2\eta_T} = \frac{F_T g_0 I_{sp}}{2\eta_T} \tag{25}$$

where F_T is the thrust, u_e is the exhaust velocity, g_0 is gravity acceleration at sea-level. The specific impulse I_{sp} is defined from $u_e = g_0 I_{sp}$. The effective panel area A_p is related to the power with the specific power per panel area a_P, which results in:

$$A_p = \frac{F_T u_e \zeta}{2\eta_T a_P \eta_{as}} \tag{26}$$

A nominal $a_P = 368$ W/m^2 is considered based on typical spacecraft solar panels [29] and a margin ζ of 1.2 is applied to account for sub-systems other than the thruster. A solar panel assembly efficiency $\eta_{as} = 0.9$ is included to account for losses resulting from assembly of multiple solar panels into larger sections [30, p. 414]. Only one array side is assumed to be exposed to direct sunlight. The total solar panel area can be larger than the arrays due to panels mounted on the entire area of the spacecraft sides A_s. In the case of GOCE, the total solar array area was composed of 4 m^2 body-mounted and 5 m^2 of wing-mounted arrays [31]. It is calculated that $1/\pi$ of the total side area could generate power at maximum efficiency using the integral of the cylindrical surface normal dot product with a reference Sun vector. A_s can be found from a specified spacecraft aspect ratio AR_s and the intake area:

$$AR_s = \frac{L}{d_i} \quad \rightarrow \quad A_s = 4AR_s A_i \tag{27}$$

where d_i is the intake diameter. The array area A_a required is therefore:

$$A_a = A_p - \frac{1}{\pi}A_s = A_p - \frac{4AR_s A_i}{\pi} \tag{28}$$

5. Drag-compensation analysis

A 1D steady-state EOM along the orbital velocity is derived for the air-breathing satellite using equilibrium of the forces shown in Fig. 4.

$$F_T cos(\alpha_t) - \dot{m}_t u_\infty - F_{D,i} - F_{D,s} - F_{D,a} = 0 \tag{29}$$

$$F_T cos(\alpha_t) - \dot{m}_t u_\infty - \frac{1}{2}\rho_\infty u_\infty^2 \left[\left(1 - \eta_c\right) C_{D,i} A_i + C_{D,s} A_s + C_{D,a} A_a \right] = 0 \tag{30}$$

- F_T is the ABEP thrust, with component $F_T cos(\alpha_t)$ along the orbital velocity. For the nominal spacecraft configuration, $\alpha_t = 0$ and so $F_T cos(\alpha_t) = F_T$.
- $\dot{m}_t u_\infty$ accounts for the deceleration of air from u_∞ to 0 velocity for thermalisation.
- $F_{D,i}$ is the intake pressure drag, due to the fraction of air $\left(1 - \eta_c\right)$ which does not pass fully through the intake to the thruster inlet. $\left(1 - \eta_c\right) A_i$ is therefore the effective frontal surface encountered by the onset flow.

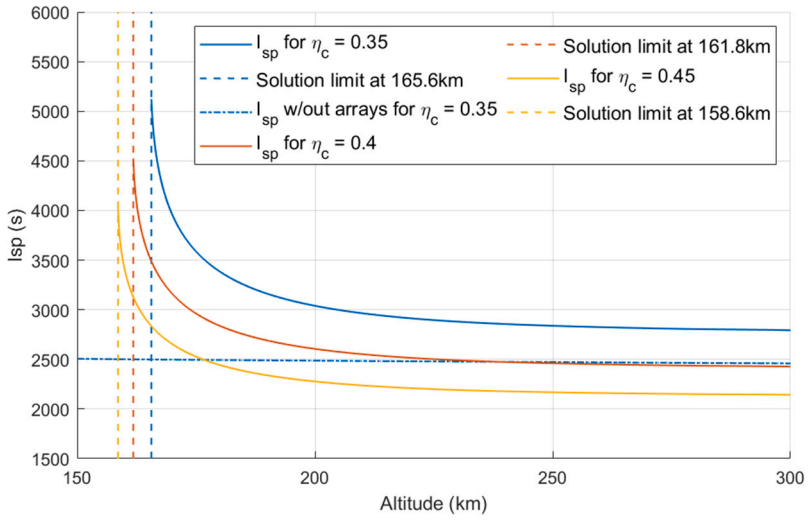

Fig. 13. I_{sp} solution with altitude for varying η_c.

Table 4
Input variables for simulations.

$\phi = 0°,\ \psi = 0°$	$AR_s = 3$
$\theta = 0°,\ \theta_a = 0°$	$T_{max} = 400$ K
$\eta_c = 0.35,\ AR_i = 14$	$n_{t,lim} = 10^{18}$ m^{-3}
$a_P = 368$ W/m^2, $\zeta = 1.2$	$F10.7 = 140,\ Ap = 15$
$\eta_T = 0.5,\ \eta_{as} = 0.9$	Date: 01/01/00

- $F_{D,s}$ and $F_{D,a}$ are the drag terms for the spacecraft sides and solar arrays respectively.

Using the following relations:

$$F_T = \dot{m}_t u_e \qquad \eta_c = \frac{\dot{m}_t}{\dot{m}_\infty} = \frac{F_T}{u_e}\frac{1}{\rho_\infty A_i u_\infty} \qquad A_i = \frac{F_T}{u_e \eta_c \rho_\infty u_\infty} \tag{31}$$

A quadratic equation in u_e is obtained from Eq. (30):

$$\left[\frac{C_{D,a}\rho_\infty u_\infty^2 \zeta}{4 a_P \eta_{as} \eta_T}\right] u_e^2 + [-1]\, u_e + \left[u_\infty \left(1 + \frac{C_{D,i}\,(1-\eta_c)}{2\eta_c} + \frac{2C_{D,s}AR_s}{\eta_c} - \frac{2C_{D,a}AR_s}{\pi\eta_c}\right)\right] = 0 \tag{32}$$

Eq. (32) reveals that drag compensation is purely dependent on the efficiencies of the intake, solar panels and thruster, and the actual F_T value is unimportant. The simulation input parameters used to obtain the results presented in the following section are shown in Table 4, unless otherwise noted. This approach models exact drag compensation (i.e. $F_T = F_D$), therefore the results shown below should be seen as the effective values required from the thruster to operate at a given altitude.

The equation of motion solution derived above can be compared to the formulation of [25] where drag from the solar array and spacecraft sides is neglected. This gives the same result as Eq. (32) but without the terms containing $C_{D,a}$ and $C_{D,s}$. The solutions for three values of η_c are shown against altitude in Fig. 13. Here I_{sp} is plotted instead of u_e as it is more commonly used as a metric for thruster performance. The solid line is the solution of Eq. (32) which, for the nominal $\eta_c = 0.35$, is compared to the horizontal dash–dot solution if neglecting array or side drag.

For a given η_c, the full solution tends to the dash–dot curve at higher altitudes since less thrust is required, meaning solar array area (and so drag) diminishes, and the constant offset is purely from spacecraft side drag. However, at lower altitudes there is a significant drag component from the solar arrays needed to power the thruster and the I_{sp} must increase in order to avoid generating less thrust than drag, before reaching an asymptotic limit. The I_{sp} required from Eq. (32) has no real solution below a certain altitude, which is shown by the vertical dashed lines in Fig. 13. This result indicates that the realistic power required by the thruster I_{sp} is a significant factor in defining the lower altitude limit of an air-breathing satellite.

5.1. Effect of efficiencies and s/c aspect ratio

The efficiencies η_c, η_T and specific power a_P together represent the properties of the satellite as a system, and these values control the I_{sp} solution. The collection efficiency η_c has the most significant effect. An increased η_c lowers both the I_{sp} required at a given altitude and the altitude at which a real solution no longer exists. This is because a higher η_c leads to a larger $\dot{m}_t$ and therefore more thrust. Maximising η_c is vital for an air-breathing satellite to access lower altitude orbits, however a high η_c results in a reduced β and so a reduced upper altitude limit. The intake design can therefore shift the operating range towards lower or higher altitudes but both cannot be simultaneously achieved with a passive intake.

The effect of η_c is shown in Fig. 14(a) on the lower and upper altitude limits available for I_{sp} values of 3500 s and 4500 s. The compression ratio β is shown by the dashed contours. As expected, at a given altitude, the compression ratio possible is strongly inversely dependent on the collection efficiency. Since β is only a function of η_c, it does not vary with I_{sp}, and so the upper altitude limit curve is fixed. A feasible scenario, where the upper limit is higher than the lower value, is shown as the shaded patch in the figure. A higher I_{sp} value brings down the lower altitude limit, allowing flight at reduced η_c. The variation of the altitude range (height of the shaded patch in Fig. 14(a)) with η_c and I_{sp} is shown in Fig. 14(b). For instance, an $I_{sp} = 3500$ s results in a feasible range for $\eta_c \approx 0.3$–0.57. An increase in I_{sp} gives a larger total altitude range, which occurs at lower values of η_c where improved compression is possible.

The total thruster efficiency η_T and array specific power a_P produce a similar effect on the solution, as an increase in both corresponds to a smaller array area. This therefore lowers the minimum altitude limit for the solution and the I_{sp} required. However, the impact of η_T and a_P is less significant than η_c as they only affect the solar array drag term. A combination of low $\eta_c = 0.35$ and high $AR_i = 14$ is used for the simulations in this analysis as priority is given to maximising the intake compression, and therefore increasing the altitude at which the minimum air density limit occurs. This intake performance, giving $\beta \approx 100$ at this altitude as shown in Fig. 12, is within the limits assumed by other studies, such as Andreussi et al. [11] who estimate β as 95–140.

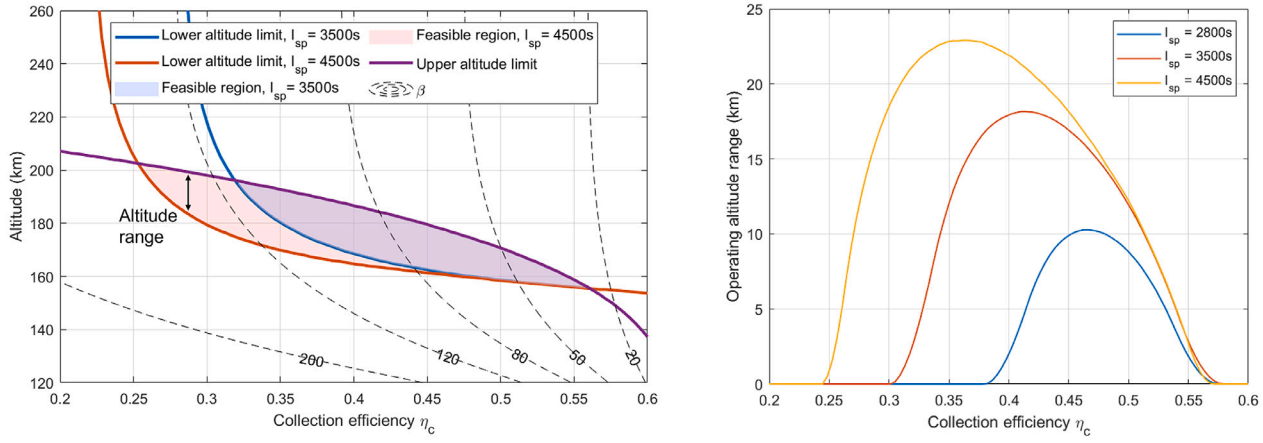

(a) Upper and lower altitude limits, showing feasible range.

(b) Operating range possible with I_{sp}.

Fig. 14. Effect of η_c on β and operating altitudes with varying I_{sp}.

5.2. ABEP operating flight envelope

The operating altitude can be expressed as a function of the generic thruster performance figures: I_{sp} and T/P, which represent the propellant and power usage of the thruster respectively. This link between thruster performance and feasible operating altitude is shown in Fig. 15(a), in which the altitude contours are solutions to the drag compensation formulation of Eq. (32). The altitude corresponding to a minimum density of $n_{t,lim} = 10^{18}$ m^{-3} at the thruster channel is shown in red, here it is 193.2 km. Since the ABEP spacecraft would have to operate at altitudes below this value, the envelope of required thruster performance can be identified. For these spacecraft, intake and simulation parameters, a minimum I_{sp} of around 3000 s and minimum T/P of around 8 mN/kW are required. A reduced performance level can be tolerated if the minimum air density required for thruster operation is lowered, so feasible drag-compensation could occur at higher altitude values.

Fig. 15(b) shows the same feasible altitude boundaries as Fig. 15(a) with overlapped lines at constant thruster efficiency values, allowing identification of η_T required for feasible ABEP flight. Due to the model formulation, it is possible to conjointly define the parameters of the ABEP spacecraft for a given thruster power. Figs. 15(c) and 15(d) show the thruster mass flow rate and intake area respectively for $P_t = 1$ kW, and both these values scale linearly with thruster power. It should be noted that this drag-compensation analysis is based on average atmospheric properties at each altitude, which are calculated by averaging across a range of evenly distributed latitudes and longitudes along a dawn–dusk SSO trajectory, as well as an evenly distributed set of times of day and days of year. For this analysis, the average atmospheric properties are calculated from a set of 20 latitude–longitude combinations, which are then evaluated and averaged over first 10 times of day and lastly 10 days of year. The assumptions included in the drag-compensation analysis presented in this Section are summarised in Table 5. A more refined atmospheric and orbital model, incorporating time-accurate variability into the orbital dynamics propagation, is implemented in the next stage of analysis in Section 6.

6. Orbit propagation of ABEP spacecraft

6.1. Performance of existing thrusters with atmospheric propellants

The performance data for existing thrusters operated with atmospheric gases as propellant is analysed to indicate the altitude range possible. The data of Cifali et al. [32] and Lotz et al. [33] is used here, in which the RIT-10-EBBM prototype was tested with xenon, oxygen, nitrogen and a mixture of the latter two. The tests show the thruster can be operated at a certain thrust level using a range of propellant flow rates, resulting in varying thruster power and therefore changing I_{sp} and T/P with flow rate. A reference operating point was calculated for the thruster operation with each propellant using the maximum power value, which is shown in Table 6. The variation of I_{sp} and T/P with flow rate is shown in Fig. 16 for the RIT-10-EBBM with a mixture of $0.56N_2$+$0.44O_2$ to replicate the gas element composition at a 200 km VLEO altitude. Given that the design of the RIT-10-EBBM is optimised for xenon, it is likely that the significant drop in η_T and T/P between operation with Xe and O_2 or N_2 is indicative of a reduced mass utilisation efficiency. The slight increase in I_{sp} is therefore likely a trade-off between improved acceleration due to less-massive particles and reduced effectiveness of propellant ionisation.

The performance of the RIT-10-EBBM with the N_2+O_2 mixture is promising for the development of an ABEP system, as the combination of I_{sp} and T/P is within the feasible operating region defined in Fig. 15(a). This predicts that operation is possible at an altitude of around 180 km. However, the results of the drag-compensation model are based on averaged atmospheric properties at each altitude and therefore do not account for the variability of the atmosphere, which can be significant even over the course of a single orbit. Given that drag-compensation is evaluated at each altitude, the results also assumes a circular orbit for the air-breathing spacecraft. While this is a useful representation for an initial design-tool, it is informative to propagate the orbital motion of a given ABEP spacecraft in order to observe the coupled nature of spacecraft thrust, altitude and properties of the onset airflow. This analysis takes into account the high level of variability in VLEO atmospheric properties as well as the perturbations introduced into the orbital altitude due to the non-spherical harmonics of the Earth's gravity field.

The use of test data is a stringent way of simulating the thruster performance for the propagation. Experimental data at a thrust level of 7.16 mN is only available for an $\dot{m}_t$ range of 5–16 sccm, or equivalently 0.11–0.36 mg/s for the tested $M = 30$ g/mol [33]. For the propagations, the lower limit is set to 6sccm (or 0.13mg/s) due to the excessively low effective T/P ratio of the data points at the lowest end of the mass flow rate range leading to inefficient thruster operation. For larger onset flow rate values in the simulation, $\dot{m}_t$ is limited to the maximum tested 0.36 mg/s. The spacecraft arrays are sized for the $P_t = 560$ W reference operating point in Table 6, which is the maximum power of the selected range. A solar panel specific power of 368 W/m^2 and assembly efficiency of 0.9 (or equivalently total efficiency of 0.24) is used for the simulations and a margin of 20% added on top of P_t to account for additional spacecraft sub-systems, resulting in a total

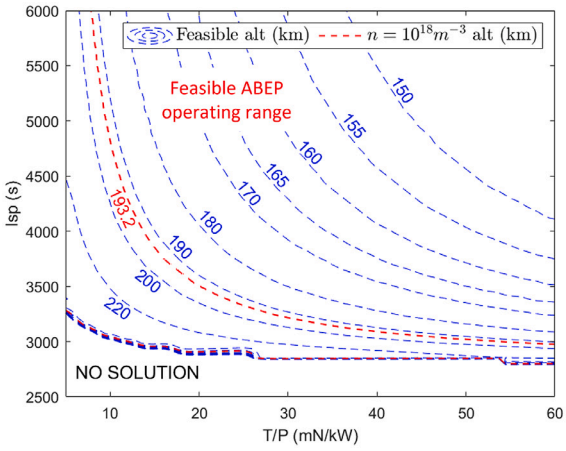

(a) Feasible altitude vs thruster I_{sp} and T/P.

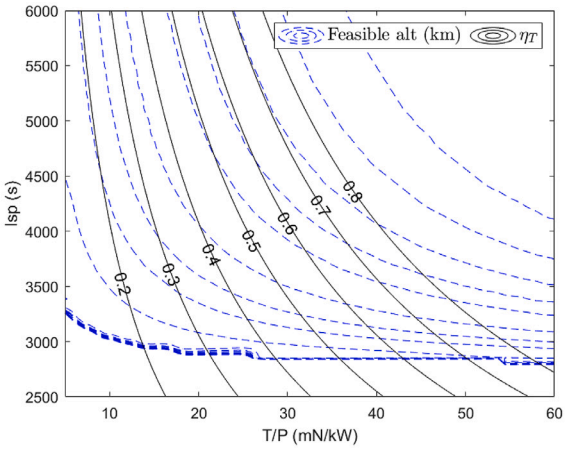

(b) Thruster η_T vs I_{sp} and T/P, overlapped with feasible altitude boundaries (from Figure 15a).

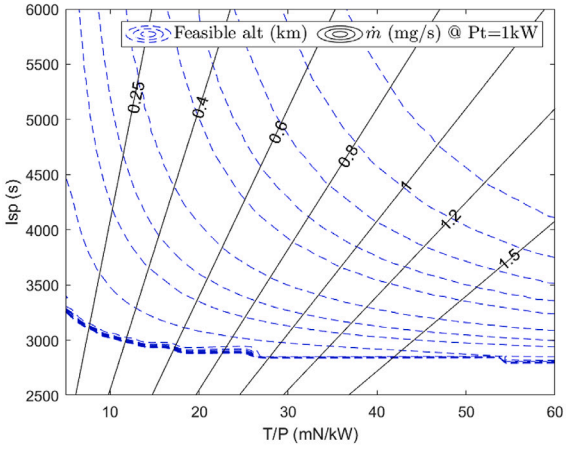

(c) Feasible thruster $\dot{m}_t$ for $P_t = 1kW$ vs I_{sp} and T/P, overlapped with feasible altitude boundaries (from Figure 15a). $\dot{m}_t$ scales linearly with thruster power.

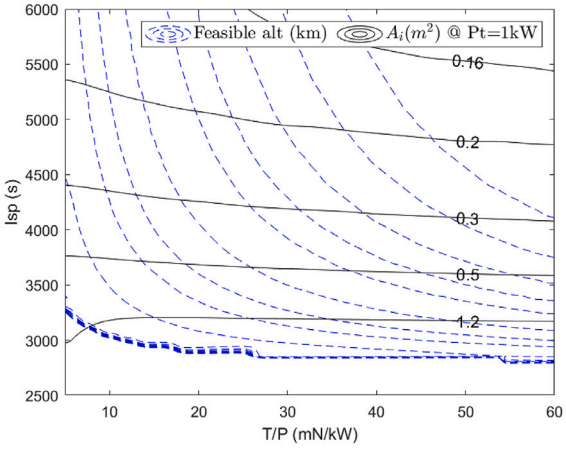

(d) Feasible A_i for $P_t = 1kW$ vs thruster I_{sp} and T/P, overlapped with feasible altitude boundaries (from Figure 15a). A_i scales linearly with thruster power.

Fig. 15. Flight envelope results from drag-compensation analysis using averaged atmospheric properties for dawn–dusk SSO.

Table 5
Summary of assumptions considered in model of Section 5.

Variability type	Variability timescale	Assumptions included
Orbital path	Short term (per orbit) Long term (seasonal)	Circular orbit (constant altitude).
Atmospheric properties	Short term (per orbit)	Averaged (at each altitude) over 20 SSO-path latitudes/longitudes and 10 evenly-distributed times of day.
	Long term (seasonal)	Averaged over 10 evenly-distributed days of year.
	Long term (solar cycle)	Fixed average solar activity.

Table 6
Reference performance of RIT-10-EBBM [32,33].

Gas mix	T (mN)	$\dot{m}$ (sccm)	P (W)	I_{sp} (s)	T/P (mN/kW)	η_T
Xe	15.1	3.2	600	4879	25.1	0.60
O_2	7.43	6.0	570	5306	13.0	0.34
N_2	6.95	6.8	610	5011	11.4	0.28
$0.56N_2 + 0.44O_2$	7.16	6.0	560	5455	12.8	0.34

effective required solar panel area of $A_p = 2.02$ m^2. The necessary intake area is identified from the drag-compensation analysis as $A_i = 0.1$ m^2, and this can be seen in Fig. 15(d) when a 0.56 scaling is applied to the $P_t = 1$ kW plot. The array area A_a is therefore 1.64 m^2 as per Eq. (28).

Since the propellant density during tests is not reported, a typical range of 10^{18}–10^{19} m^{-3} is assumed for the acceptable n_t, outside of which the thruster is modelled as inactive.

6.2. VLEO orbital conditions

The orbital profile of the air-breathing spacecraft is simulated using a high-accuracy orbit propagator with variable-timestep integration, which is able to account for high-order harmonics of the Earth's gravity and evaluate the NRLMSISE-00 atmospheric model at each timestep. The propagator results for an SSO with an initial altitude of 190 km relative to R_E were verified using the open-source General Mission Analysis Tool (GMAT) [34]. The cases compared were ones without

Table 7
Summary of assumptions considered in model of Section 6.

Variability type	Variability timescale	Assumptions included
Orbital path	Short term (per orbit)	Eccentric orbit due to non-spherical gravity harmonics up to order 10.
	Long term (seasonal)	Variation with seasonal effects.
Atmospheric properties	Short term (per orbit)	Variation with time-dependent altitude and solar illumination.
	Long term (seasonal)	Variation with seasonal effects.
	Long term (solar cycle)	6.2–6.6: Fixed average solar activity. 6.7: Fixed and real time-varying solar and geomagnetic activity.

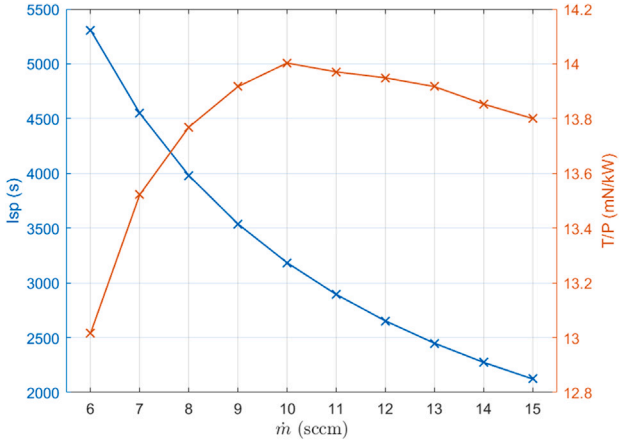

Fig. 16. Reference performance used in this study of RIT-10-EBBM with $0.56N_2$+$0.44O_2$ mixture.
Source: Calculated from test data of [33].

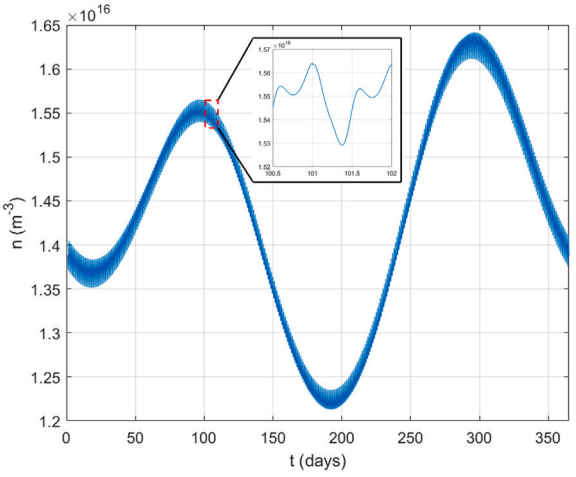

Fig. 17. Onset air density variation during year for dawn–dusk SSO at 180 km altitude relative to R_E.

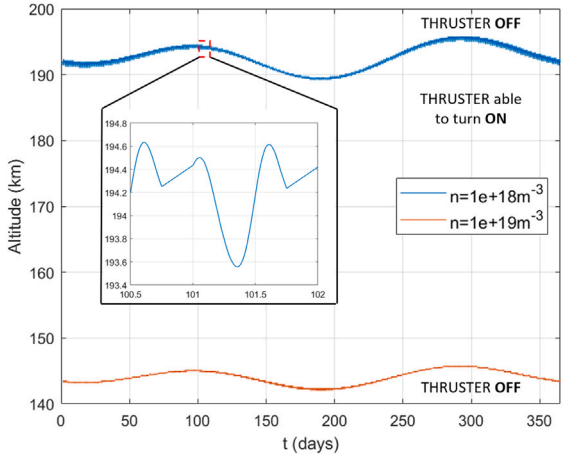

Fig. 18. Altitude (relative to R_E) variation of thruster density limits during year for dawn–dusk SSO.

thrust or drag, a constant thrust level of 5mN without drag, and drag at a constant C_D without thrust. There was very good agreement between the orbital profiles, with a discrepancy in the order of 6 m after one year without thrust or drag, and a reasonable difference of 2.5 days between re-entry times for the case with drag given that the two methods use different atmospheric models.

Due to the extremely low orbital altitude, the non-sphericity of Earth's gravity has a significant effect on the spacecraft's motion and this results in unavoidable eccentricity of the orbit. This is significant given that even a small change in altitude of several 10's km can require a considerably different level of thruster performance, as shown in Fig. 15(a). The majority of existing literature addressing ABEP mission analysis assumes a circular orbit, however this type of orbit is not naturally possible in the VLEO environment. The propagator is therefore run with gravity harmonics up to order 10 in order to capture this behaviour.

As well as the prescribed variation in altitude due to a non-circular orbit, the atmospheric properties change with time. This behaviour is shown in Figs. 17 and 18. Fig. 17 displays the particle density averaged over the trajectory of an SSO (see text of Section 5.2) and plotted with time at a representative altitude of 180 km relative to R_E. Fig. 18 shows the variation in altitude at which this average density corresponds to the thruster limits of 10^{18}–10^{19} m^{-3}. There is therefore a seasonal variation in operating altitude with a total range of around 7 km, to which the thruster must be able to adapt over the course of the year.

The assumptions included in the time-propagated analysis presented in this Section are summarised in Table 7.

6.3. Initial frozen orbit

It is desirable to avoid large variations in atmospheric properties due to changes in altitude driven by orbital eccentricity, as this will result in the thruster spending significant parts of the orbit outside of the operating range for collecting a sufficiently high flow rate $\dot{m}_t$ and density at the thruster n_t, thus jeopardising the spacecraft's ability to compensate drag. A frozen orbit is therefore used to initialise the spacecraft in an orbit with reduced eccentricity and one which is stable over the long-term, at least when negating the effects of thrust and drag. This can be done with a semi-analytical method when accounting for the J_2 and J_3 zonal gravity harmonics. Here the process of Rosengren [35] is followed to derive an expression, based on minimising the drift of argument of periapsis $\bar{\omega}$ ($d\bar{\omega}/dt = 0$), that links the mean orbital elements of semi-major axis $\bar{a}$, eccentricity $\bar{e}$ and inclination $\bar{i}$:

$$1 + \frac{J_3 R_E}{2J_2\bar{a}(1-\bar{e}^2)}\left(\frac{\sin^2\bar{i} - \bar{e}\cos^2\bar{i}}{\sin\bar{i}}\right)\frac{1}{\bar{e}} = 0 \tag{33}$$

Table 8
Mean and osculating Keplerian elements.

Mean (km, rad):		Osculating (km, rad):
$\bar{a} = 6578.15515965$		$a = 6568.19021709$
$\bar{e} = 0.00112151$		$e = 0.00035740$
$\bar{i} = 1.68130795$	→	$i = 1.68139190$
$\bar{\Omega} = 0.20634295$		$\Omega = 0.20634295$
$\bar{\omega} = \pi/2$		$\omega = \pi/2$
$\bar{\Theta} = 0$		$\Theta = 0$

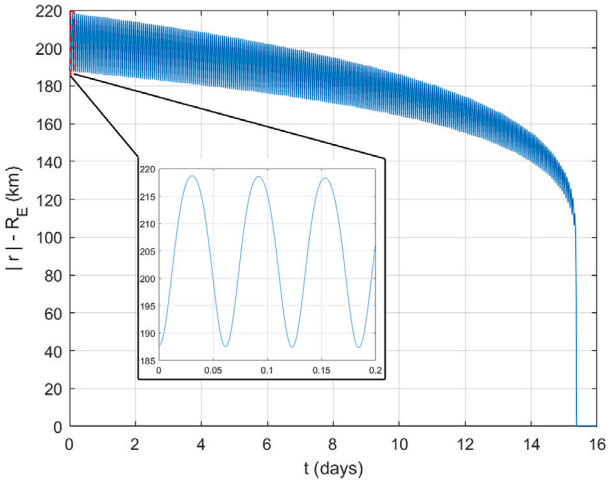

Fig. 19. Propagated altitude profile without thrust and with atmospheric drag.

Eq. (33) is combined with the SSO condition on the time derivative of the mean Right Ascension of the Ascending Node (RAAN) $\dot{\bar{\Omega}}$ equal to a precession of 360°/sidereal year, accounting for the J_2 term:

$$\frac{-3J_2R_E^2\cos\bar{i}}{2(1-\bar{e}^2)^2\,\bar{a}^{7/2}} - 1.99096871\times10^{-7} = 0 \tag{34}$$

Eqs. (33) and (34) are solved simultaneously to provide a set of mean initial orbital elements for each altitude. It was found that an ω around 90° resulted in a minimal orbit eccentricity, so this is combined with a true anomaly $\Theta = 0$ to give an initial spacecraft location approximately over the North Pole. In order to ensure that the initial orbital motion matches the solution, the mean orbital element set is transformed to osculating elements using Brouwer–Lyddane theory [36,37]. The long version of the transformation is used which considers both the short period, on the length of the orbit, and long period motion, on the length of the periapsis rotation, terms with zonal harmonics from J_2 to J_5 and including J_2^2. This results in the Keplerian orbital element set shown in Table 8.

A spacecraft mass of 200 kg is used for the propagations that follow as a representative value for the spacecraft size, given that the spacecraft dimensions are an intake diameter of 0.36 m, a length of 1.1 m ($AR_s = 3$) and a total array span of 1.89 m ($A_a = 1.64$ m^2 and assuming full body-length arrays). The altitude profile without thrust is shown in Fig. 19, which shows the orbital altitude relative to the equatorial Earth radius ($|r| - R_E$). The eccentricity due to non-spherical gravity is indicated by the immediate periapsis–apoapsis range of 30 km. Since there is no thrust, the intake drag term is calculated with $\eta_c = 0$ so as to simulate the worst-case scenario that none of the onset air passes through the thruster. Re-entry occurs after 15 days in this case.

6.4. Uncontrolled thruster behaviour

The inclusion of the thruster as per the data of the RIT-10-EBBM with N_2+O_2 acts to extend the time on orbit. This is shown by the background profile in Fig. 20, for which the re-entry time is extended to 59 days. While this demonstrates the effectiveness of the thruster, the as-tested performance is not sufficient to raise the mean semi-major axis of the orbit at any point in the profile. An increase in thruster T/P is therefore introduced, which has the effect of reducing the array area (and so array drag) while keeping the remaining thruster parameters unchanged. The aim of this approach is to investigate how much of an increase in performance is required to sustain a stable altitude profile.

The result of an improvement in T/P to 19 mN/kW is shown as the foreground curve in Fig. 20, which is the equivalent of an increase in η_T to 0.51. This results in the ability of the thruster to successfully raise the mean semi-major axis over time and so further extends the profile up to a re-entry time of 88 days. However, a divergent altitude behaviour is identified after approximately 60 days. The effect of the thruster is clearly visible at this time by the increasing orbit apoapsis, however there is a simultaneous decay in periapsis which is not corrected by the thruster firings. This leads to a rapidly diverging altitude range that is unrecoverable since the descending periapsis incurs high levels of drag, and this prompts re-entry after around 20 further days. The reason for this behaviour is shown by the closeup of Fig. 20, in which the altitude profile is plotted as a continuous line for periods of thruster firing and in cross markers when the thruster is idle. The thruster is seen to only turn on around the periapsis of the orbit, when the density and mass flow rate values are above the minimum level. Since an applied thrust affects the orbit radius at a point 180° from the current location, this thruster behaviour lifts the apoapsis, while the periapsis continues to fall since the thruster does not function in the higher regions of its orbit.

It is possible to establish a stable altitude profile with an uncontrolled thruster, however only at very large spacecraft mass values. Stability is improved for higher T/P values however at the maximum simulated thruster performance of $T/P = 23$ mN/kW, the orbit is stable after 500 days only for masses above 1000 kg. The effect of spacecraft mass is discussed in more detail in Section 6.6. In all cases with an uncontrolled thruster, and even for a stable configuration, an oscillatory behaviour is periodically present in the altitude profile due to thrusting occurring predominantly around periapsis. This can be seen in Fig. 21, which shows that the instantaneous periapsis–apoapsis altitude range reaches a maximum of around 70 km despite a profile that is stable in the long-term.

6.5. Controlled thruster behaviour

A thruster controller is used to avoid the previously identified divergent altitude behaviour. The design approach for this controller is to prevent the thruster from firing around the periapsis of the orbit, which is based on an evaluation of mean orbital elements at each thruster timestep. The control variable is formulated as shown below and compared to a control target CT:

$$\begin{aligned} \frac{|r| - \bar{r}_p}{\bar{r}_a - \bar{r}_p} < CT \quad &\rightarrow \quad \text{Thruster OFF} \\ \frac{|r| - \bar{r}_p}{\bar{r}_a - \bar{r}_p} > CT \quad &\rightarrow \quad \text{Thruster ON} \end{aligned} \tag{35}$$

The control variable is a measure of the proximity of the current spacecraft position to the mean orbit periapsis, as a ratio of the periapsis to apoapsis range. Therefore, if $CT = 0.1$, the thruster is prevented from firing if its altitude is within 10% of the current periapsis value. The thruster firings are therefore based on both a correct $\dot{m}_t$ and n_t regime, as well as the control variable, and this strategy is shown in Fig. 22. The thruster does not fire around apoapsis due to insufficient $\dot{m}_t$ and does not fire around periapsis due to the control variable.

The use of the controller described above is effective in avoiding the divergent altitude behaviour and this achieves a stable, minimised, long-term altitude range. This is shown in Fig. 23(a), which is a propagation of the orbital altitude over a two-year period. The controller achieves a minimised altitude range of 10–15 km, with a minimum operating altitude of 157 km and a maximum of 181 km relative to

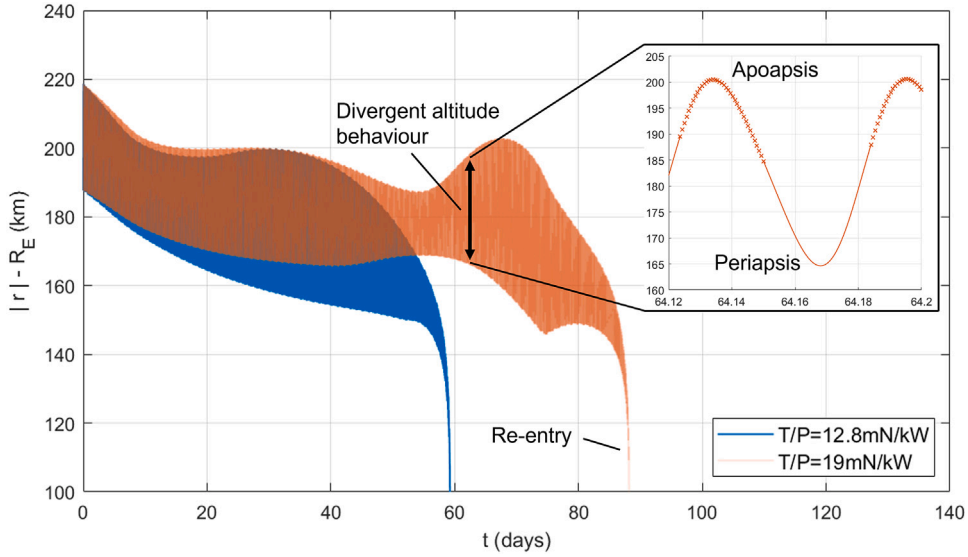

Fig. 20. Propagated altitude profile of uncontrolled thruster for 200 kg s/c mass, showing effect of increased T/P from 12.8 mN/kW ($\eta_T = 0.34$) to 19 mN/kW ($\eta_T = 0.51$). On closeup: solid line indicates thruster ON, crosses indicate thruster OFF.

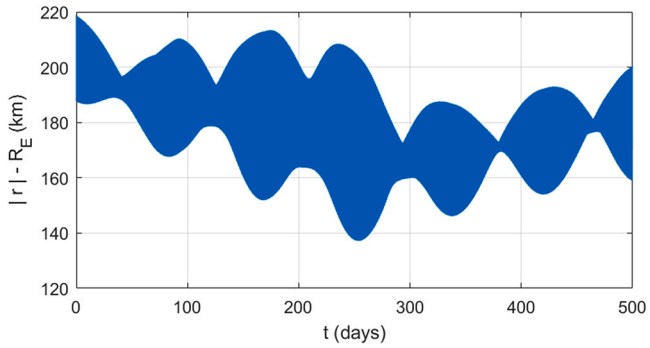

Fig. 21. Propagated altitude profile for uncontrolled thruster with $T/P = 23$ mN/kW and 1000 kg s/c mass.

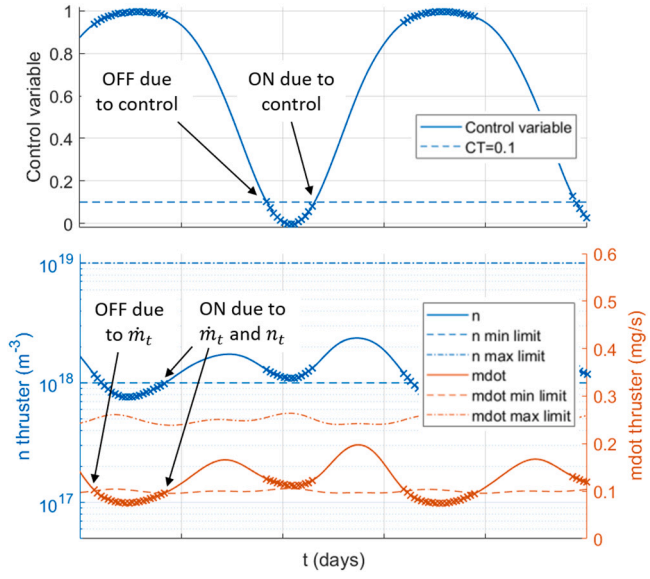

Fig. 22. Thruster firing based on control variable, $\dot{m}_t$, n_t. Solid line indicates thruster ON, crosses indicate thruster OFF.

the equatorial Earth radius. This translates to a geodetic altitude range between 161 km and 201 km, which represents the height of the spacecraft above the surface of the WGS 84 Earth ellipsoid model and is the key value in determining the atmospheric properties. This is shown in Fig. 23(b). The range corresponds well to the approximate value of 180 km predicted by the drag compensation analysis (Fig. 15(a)). After an initial descent from the starting $\bar{a} = 200$ km and subsequent settling period, the long-term variation of the altitude follows the seasonal variation in average density that is also shown in Fig. 23(a).

6.6. *Effect of spacecraft mass*

The propagation analysis reveals the significant impact of spacecraft mass on the orbital profile and re-entry behaviour, as it affects the acceleration resulting from the imbalance of thrust and drag forces. In the case of no thrust, there is a linear relationship between mass and re-entry time since an increased mass results in reduced deceleration for the same orbital drag. Simulation results including the use of the ABEP system can be seen for four different T/P values in Fig. 24, where $T/P = 12.8$ mN/kW represents the unmodified value taken from test data of the RIT-10-EBBM with N_2+O_2. The results shown are based on simulations with a run time of 500 days, therefore data points reaching this y-axis maximum are those that did not undergo re-entry. In the case of no thruster control, the spacecraft is not able to achieve stable operation in the long-term, even at increased T/P values. An orbital profile past 500 days does occur for the largest mass values at high T/P, however these profiles display a monotonically decreasing $\bar{a}$ throughout the simulation, indicating that the high mass delays but does not avoid eventual re-entry when the thruster is uncontrolled.

A stable operating altitude without re-entry is achieved when thruster control is included, with $CT = 0.1$ used for the data in Fig. 24. A minimum $T/P = 17.4$ mN/kW ($\eta_T = 0.47$) is needed for long-term stability, which initially occurs only for a specific mass of 180 kg. The feasible spacecraft mass range expands with increasing T/P, growing to 140–220 kg for $T/P = 19$ mN/kW ($\eta_T = 0.51$) and the full 100–1250 kg for $T/P = 23$ mN/kW ($\eta_T = 0.62$). This indicates a trade-off between a spacecraft mass high enough to avoid an excessively large deceleration from drag and small enough to allow the applied thrust of 7.16 mN to adjust the spacecraft altitude in time to seasonal changes in the atmospheric properties. The use of thruster control is ineffective at extremely large mass values, as the time-varying oscillatory behaviour seen for uncontrolled cases is retained even if the profile is stable. This

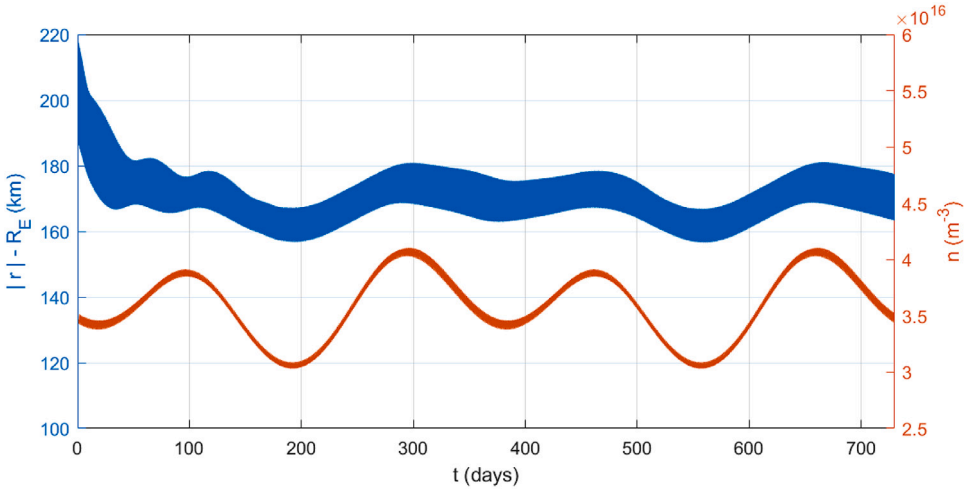

(a) Altitude relative to equatorial Earth radius and average n_∞ at 180km geodetic altitude.

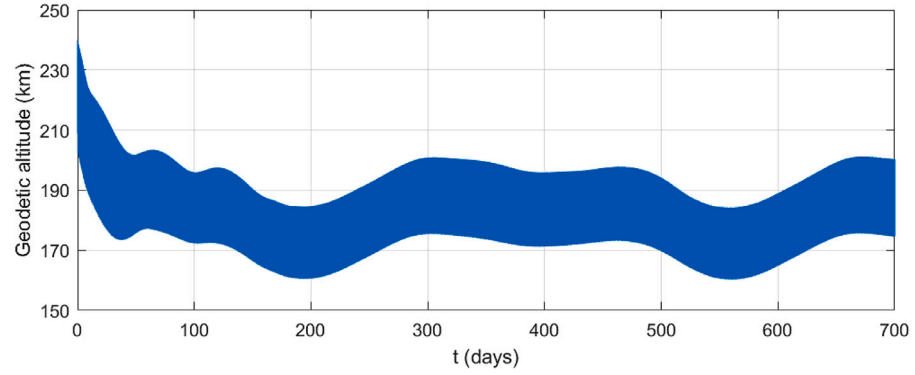

(b) Geodetic altitude.

Fig. 23. Propagated altitude profile of controlled thruster with $CT = 0.1$, 200 kg mass, $T/P = 19$ mN/kW ($\eta_T = 0.51$) and constant solar activity.

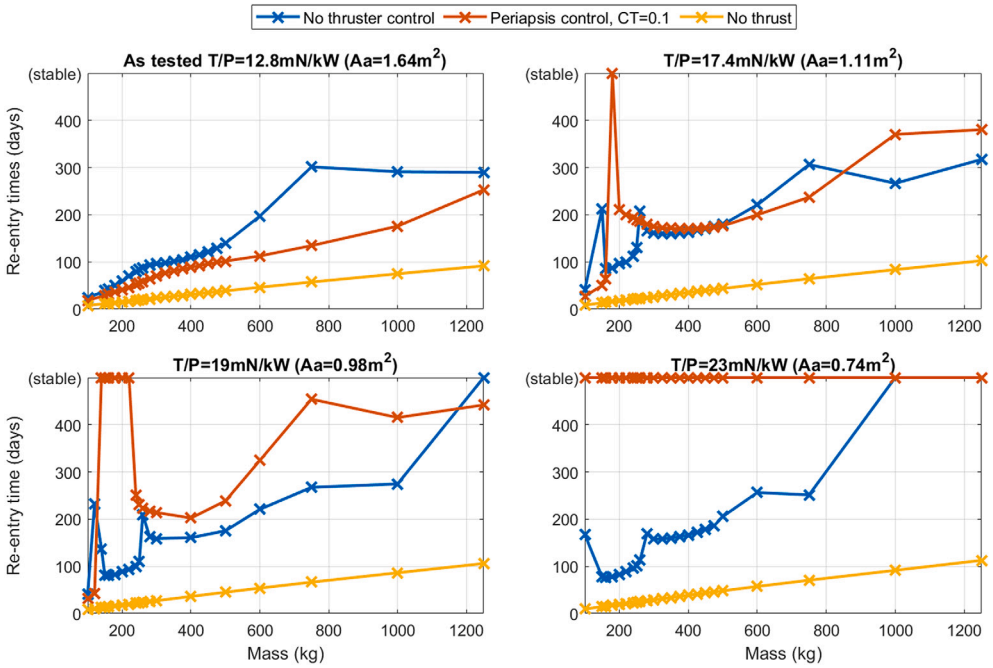

Fig. 24. Effect of spacecraft mass on re-entry time for varying control and thruster T/P. Simulated time is 500 days so cases reaching this value did not undergo re-entry (stable).

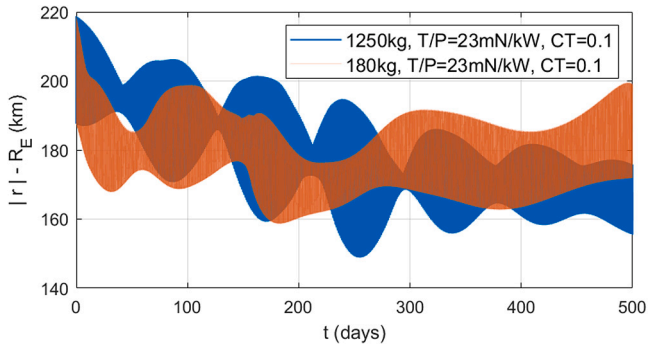

Fig. 25. Propagated altitude profiles showing effect of thruster control with $CT = 0.1$ in cases of high mass and T/P.

Table 9
Results of drag-compensation analysis with varying solar activity, using RIT-10 N_2+O_2 operating point of $I_{sp} = 5455$ s, $T/P = 12.8$ mN/kW and $P_t = 560$ W.

Solar activity	Feasible alt (km)	$n_t = 10^{18}$ m^{-3} alt (km)	A_i (m^2)	A_a (m^2)
Low	170.4	194.7	0.09	1.68
Average	180.8	193.2	0.10	1.64
High	(202.4)	194.7	0.12	1.56

*Flight altitude for high solar activity case is unfeasible as above upper n_∞ limit.

is shown by the background curve of Fig. 25. Control effectiveness with a low $CT = 0.1$ is also reduced for extremely high values of T/P, shown in the foreground curve of Fig. 25, where the periapsis–apoapsis range is expanded to 28 km at 500 days for an optimum mass of 180 kg, compared with 11 km for $T/P = 19$ mN/kW. This is due to an imbalance between the thrust and now overly-reduced drag, so a larger CT should be used to decrease the thrusting time.

6.7. Effect of solar activity

The effect of varying solar activity on the feasibility of the air-breathing spacecraft is investigated in this section. Up to this point, average solar activity values of $F10.7 = 140, Ap = 15$ have been assumed for the drag-compensation analysis and the orbit propagations. A high solar activity, modelled with $F10.7 = 250, Ap = 100$, results in a general increase of the air density and temperature at a given altitude. The density and temperature values are conversely decreased for a low solar activity, modelled with $F10.7 = 70, Ap = 8$. The results of the drag-compensation analysis performed for the three different values of solar activity are shown in Table 9, with the feasible altitude, A_i and A_a values obtained for the RIT-10-EBBM N_2+O_2 operating point. The feasible altitude at which $F_T = F_D$ is achieved increases with solar activity, however the upper altitude limit based on a minimum propellant density does not vary as significantly. For instance, the average altitude limit increases from 193.2 km to 194.7 km between medium and high solar activity, compared to a corresponding feasible altitude increase of more than 22 km. The greater density resulting from a higher solar activity would suggest a significant rise in the upper altitude limit, however the improved density at a given altitude is balanced by a decrease in the compression achieved by the intake. This occurs due to a higher onset air temperature at high solar activity, which increases the enthalpy and therefore reduces the stagnation compression ratio (see Eq. (23)). A lower β_0 reduces the β value which can be achieved, as per Eq. (24). For example, the average T_∞ at a geodetic altitude of 180 km increases from 870 K to 1130 K between average and high solar activity, leading to a decrease in β from 110 to 75.

The results in Table 9 indicate that operation at high solar activity with an unmodified $T/P = 12.8$ mN/kW is not feasible since the $F_T = F_D$ operating altitude of 202.4 km is above the 194.7 km upper altitude limit. The T/P would therefore need to be increased to allow the operating altitude to be lowered into the feasible region. The drag compensation analysis predicts that $T/P > 16$ mN/kW is required to achieve this for a fixed I_{sp}. This indicates that an additional T/P increase is needed on top of the modified values required for stable propagation when accounting for the real, time-varying solar activity.

The orbital propagations up to this point have used a fixed average solar activity value, thus long-term variations of the atmospheric properties have been due to seasonal changes with a year-long period. A simulation of the thruster response to time-varying solar activity is a more complete test for air-breathing feasibility. The 500-day simulated period from early 2000 straddles a period of medium to high solar activity, as can be seen via the $F10.7$ and Ap indices in Fig. 26. The real activity is therefore noticeably higher than the commonly assumed average values used so far.

The periapsis thruster control is found to be effective at establishing a stable altitude range in the case of time-varying solar activity. An increase in T/P and CT up to 23 mN/kW and 0.2 respectively is required, compared with the case at average solar activity for which stable operation is achieved with $T/P = 19$ mN/kW and $CT = 0.1$, since the thruster needs to achieve drag-compensation at solar activity values above the average and to respond to more rapidly-varying atmospheric properties. Both the propagated profile and variation of average density at a 180 km geodetic altitude are shown in Fig. 27(a). The resulting altitude profile is similar to the previous case using fixed, average solar activity, with a range of 9–14 km occurring at altitudes of 160–183 km relative to the equatorial Earth radius. This corresponds to a geodetic altitude in the range of 163–200 km, shown in Fig. 27(b). The stable profile demonstrates the ability of a combination of thruster control, increased T/P and an initial frozen orbit to provide robustness against variability of the atmospheric properties with time. For instance, $A_i = 0.1$ m^2 stays constant throughout the simulation even though this value is not an efficient intake sizing for all solar activities, as indicated in Table 9.

The results of the time-propagated analysis highlights several key aspects for a feasible air-breathing spacecraft:

- The thruster control law presented in this study, based on the evaluation of mean orbital elements to prevent the thruster firing around the orbit periapsis, is effective in establishing a long-term stable operating altitude. It prevents the thruster from developing a divergent altitude behaviour which results in re-entry and has been shown to function for varying atmospheric properties based on changes induced by seasons and solar activity.
- A stable operating profile can be established based on the test data of an existing Xe-designed thruster operated with atmospheric propellants, in this case the RIT-10-EBBM. The effectiveness of the drag-compensation analysis as an initial design tool is demonstrated, indicating that operation with the combination of nominal I_{sp} and T/P is feasible and sizing the intake area required. Stable operation is achieved through the use of a control law, an initial frozen orbit and an increase in the T/P above the tested value. For a 200 kg spacecraft, an increase from 12.8 mN/kW up to 23 mN/kW is required given realistic variability of the atmospheric properties during a period of medium-high solar activity. In other terms, this implies a total thruster efficiency increase from 0.34 to 0.62. The 23 mN/kW configuration corresponds to a spacecraft power of 370 W and so power density of 1.9 W/kg. This is within the same order as the 1.5 W/kg of GOCE (1.6 kW power and 1080 kg wet mass) and 1.8 W/kg of SLATS (700 W power and 380 kg wet mass) missions [31,38]. It is expected that a T/P increase is required above the results given by the drag-compensation analysis since there are significant periods of a realistic, eccentric orbit where the thruster cannot fire due to air density and mass flow limitations, and this period is only

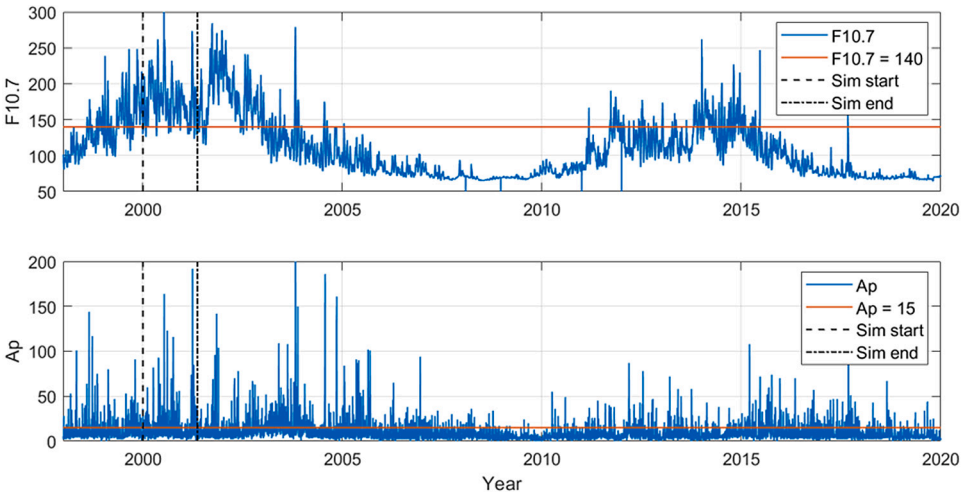

Fig. 26. $F10.7$ and Ap index variation with time.

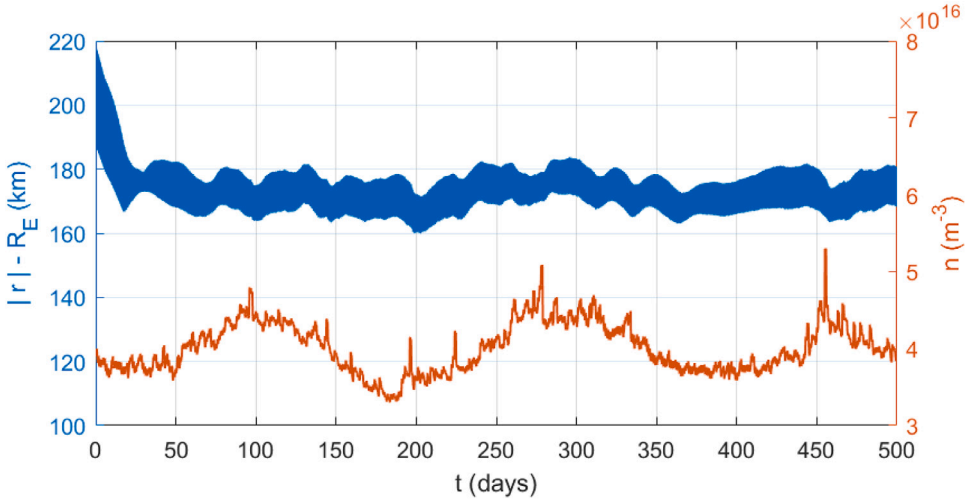

(a) Altitude relative to equatorial Earth radius and average n_∞ at $180km$ geodetic altitude.

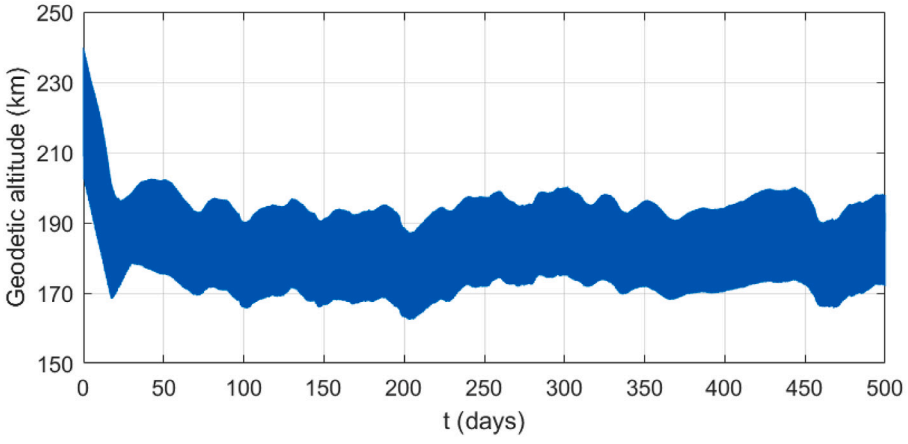

(b) Geodetic altitude.

Fig. 27. Propagated altitude profile of controlled thruster with $CT = 0.2$, 200 kg mass, $T/P = 23$ mN/kW ($\eta_T = 0.62$) and time-varying solar activity.

increased by the use of thruster control. The RIT-10-EBBM results bode well for the development of an ABEP spacecraft, since an I_{sp} in the correct level has been demonstrated and the thruster T/P can be increased with thruster design and optimisation for air rather than xenon. The thruster developed for the AETHER project aims to achieve this through the use of a successive ionisation and acceleration stage design [12]. Alternatively, a decrease in the minimum air density required for thruster operation below

the 10^{18} m^{-3} assumed here would allow flight at higher altitudes where a reduced thruster performance is feasible. The quadratic shape of the solution in Fig. 13 suggests this should be pursued even at the expense of increased power for ionisation.
- The altitude profile is dependent on the spacecraft mass, with a particular mass range for which the thruster is effective in achieving a stable operating altitude due to the trade-off between controllability and resistance to drag perturbation. An initially narrow range of feasible mass values is widened with an increase in the T/P of the controlled thruster.

7. Conclusion and further work

The drag compensation analysis highlights the importance of drag from surfaces aligned parallel to the flow, such as the arrays and spacecraft sides. This results in a quadratic solution for specific impulse with altitude to achieve drag-compensation, using atmospheric properties that are averaged at each altitude. A relationship is therefore found between normalised thruster performance and feasible operating altitude, which is combined with an upper altitude limit based on a minimum required air density at the thruster to identify the thruster performance envelope for a feasible ABEP spacecraft. For realistic intake and spacecraft values, a minimum I_{sp} of 3000 s and T/P of 8 mN/kW are required for operation below the upper altitude limit of 193 km relative to the equatorial Earth radius. The model formulation results in the ability to size the spacecraft with thruster performance, based on the area of intake and arrays required which scale linearly with thruster power.

The propagation of an air-breathing spacecraft's profile with time highlights the unavoidable orbit eccentricity introduced due to the effect of non-spherical gravity in VLEO, which results in variable altitude and flow properties over the orbit. The performance data of the RIT-10-EBBM thruster tested with a mixture of atmospheric propellants is used for the altitude propagations as a robust method of assessing the feasibility of an air-breathing spacecraft. The thruster reference operating point is $I_{sp} = 5455$ s and $T/P = 12.8$ mN/kW at $P_t = 560$ W, with limits imposed for mass flow rate and propellant density. The orbital simulations show a divergent altitude behaviour which results in re-entry, and this is addressed with a thruster control law aiming to prevent thruster firing around the orbit periapsis. A combination of an initial frozen orbit, the thruster control law and an increased thrust to power ratio above the tested value is successful in establishing a stable, long-term operating altitude, despite time-varying atmospheric properties due to changing seasons and solar activity. A spacecraft mass of 200 kg, initial mean semi-major axis altitude of 200 km relative to the equatorial Earth radius, thruster control within 20% of the periapsis as a ratio of the periapsis–apoapsis range and $T/P = 23$ mN/kW results in an altitude range of around 10 km, which occurs at altitudes of 160–183 km relative to the equatorial Earth radius. This bodes well for the development of the AETHER ABEP system. The following future work is identified:

- The model in this study assumes a fixed intake collection efficiency, however this will realistically vary at different altitudes and thrust levels due to variable air transmittance values. The model accuracy would therefore be improved if this variability was included.
- A major challenge of the ABEP system is to achieve a high ionisation efficiency with a gas mixture that varies significantly at different altitudes. Moving away from a strict interpolation of a tested data set would allow scaling of the thruster ionisation efficiency, and so performance, with the composition and molecular mass of the onset airflow.
- The effect of eclipses on available thruster power should be taken into account, which occur for a short fraction of the orbital period during some parts of the year for a dawn–dusk SSO at the altitude range in question.
- The effect of varying solar activity should be evaluated over the course of a full solar cycle. However, the simulations show that feasibility is more easily achieved during periods of low solar activity, and therefore the fact that the propagations are conducted for a period of relatively strong solar weather indicates that the long-term stability demonstrated should not be affected.
- The thruster control law can be improved to adjust to the current atmospheric conditions rather than using a fixed value for the entire simulation. This is expected to reduce the altitude range further and decrease losses of firing time, allowing more relaxed requirements on the thruster performance.

Declaration of competing interest

The authors declare that they have no known competing financial interests or personal relationships that could have appeared to influence the work reported in this paper.

Acknowledgements

This work has been partly performed within the AETHER project, funded by the European Union's Horizon 2020 research and innovation programme under grant agreement No 870436. This reflects only the author's view and the European Commission is not responsible for any use that may be made of the information it contains. The authors thank M. Smirnova at TransMIT GmbH for advice on the RIT-10-EBBM thruster test data and Professor K. Fujita of JAXA for fruitful discussion. M. Tisaev thanks the Doctoral College of the University of Surrey for his Ph.D. scholarship.

References

[1] N Crisp, et al., The benefits of very low earth orbit for earth observation missions, Prog. Aerosp. Sci. 117 (2020) 100619, URL https://doi.org/10.1016/j.paerosci.2020.100619.
[2] AETHER project consortium, 2021, AETHER. URL https://aether-h2020.eu.
[3] K Fujita, Air intake performance of air breathing ion engines, J. Japan Soc. Aeronaut. Space Sci. 52 (610) (2004) 514–521, URL https://www.jstage.jst.go.jp/article/jjsass/52/610/52_610_514/_article/-char/ja/.
[4] K Fujita, Air intake performance estimation of air-breathing ion engines, Trans. Japan Soc. Mech. Eng. 70 (700) (2004) 3038–3044, URL https://www.jstage.jst.go.jp/article/kikaib1979/70/700/70_700_3038/_article.
[5] D Di Cara, J Gonzalez del Amo, et al., RAM electric propulsion for low earth orbit operation: an ESA study, in: 30th International Electric Propulsion Conference, Florence, Italy, 2007, URL http://electricrocket.org/IEPC/IEPC-2007-162.pdf.
[6] F Romano, T. Binder, et al., Air-intake design investigation for an air-breathing electric propulsion system, in: 34th International Electric Propulsion Conference, Hyogo-Kobe, Japan, 2015, URL http://electricrocket.org/IEPC/IEPC-2015-269_ISTS-2015-b-269.pdf.
[7] F Romano, B Massuti-Ballester, et al., System analysis and test-bed for an atmosphere-breathing electric propulsion system using an inductive plasma thruster, Acta Astronaut. 147 (2018) 114–126, URL https://doi.org/10.1016/j.actaastro.2018.03.031.
[8] F Romano, System Analysis and Test Bed for an Air-Breathing Electric Propulsion System (Master's thesis), Aerospace Eng., University of Padua and Universitat Stuttgart, 2014.
[9] S Barral, G Cifali, et al., Conceptual design of an air-breathing electric propulsion system, in: 34th International Electric Propulsion Conference, Hyogo-Kobe, Japan, 2015, URL https://www.academia.edu/14207093/Conceptual_Design_of_an_Air-Breathing_Electric_Propulsion_System.
[10] T Andreussi, et al., Development and experimental validation of a hall effect thruster RAM-EP concept, in: 35th International Electric Propulsion Conference, Atlanta, USA, 2017, URL http://electricrocket.org/IEPC/IEPC_2017_377.pdf.
[11] T. Andreussi, et al., Development status and way forward of SITAEL's air-breathing electric propulsion engine, in: AIAA Propulsion and Energy Forum, Indianapolis, USA, 2019, URL https://doi.org/10.2514/6.2019-3995.
[12] E Ferrato, et al., Development roadmap of SITAEL's RAM-EP system, in: 36th International Electric Propulsion Conference, Vienna, Austria, 2019, URL http://electricrocket.org/2019/886.pdf.
[13] P Parodi, S Boccelli, et al., Study of a collector-intake system for VLEO air-breathing platforms, in: 2019 International Conference on Flight Vehicles, Aerothermodynamics and Re-Entry Missions, Monopoli, Italy, 2019, URL https://www.researchgate.net/publication/337060417_Study_of_a_collector-intake_system_for_VLEO_air-breathing_platforms.

[14] Alenia Spazio, GOCE system critical design review (CDR), 2005, URL http://esamultimedia.esa.int/docs/GOCE_System_Critical_Design_Review.pdf.
[15] ESA, ECSS-E-ST-10-04C Rev.1 Space engineering. Space environment. ESA-ESTEC, Noordwijk, Jun 2020. URL https://ecss.nl/standard/ecss-e-st-10-04c-rev-1-space-environment-15-june-2020/.
[16] National Oceanic and Atmospheric Administration, Space weather conditions, 2021, URL https://www.swpc.noaa.gov/.
[17] J Hilsenrath, et al., Tables of Thermal Properties of Gases, National Bureau of Standards Circular 564, 1955, URL https://doi.org/10.1002/aic.690020431.
[18] S Schaaf, P Chambre, Flow of Rarefied Gases, first ed., Princeton University Press, 1958.
[19] G Bird, Molecular Gas Dynamics and the Direct Simulation of Gas Flows, second ed., Clarendon Press, 1994.
[20] C Shen, Rarefied Gas Dynamics, first ed., Springer, 2005.
[21] W Sutherland, The viscosity of gases and molecular force, Philos. Mag. Ser. 5 36 (223) (1893) 507–531, URL https://doi.org/10.1080/14786449308620508.
[22] B Munson, D Young, Fundamentals of Fluid Mechanics, sixth ed., Wiley, 2009.
[23] J Anderson, Fundamentals of Aerodynamics, sixth ed., McGraw-Hill, 2016.
[24] P Stevens, H Babinsky, Low Reynolds number experimental studies on flat plates, in: AIAA SciTech, 2014, URL https://doi.org/10.2514/6.2014-0743.
[25] T Andreussi, et al., Development and experimental validation of a Hall-effect thruster RAM-EP concept, in: Space Propulsion 2018, Seville, Spain, 2018, URL https://www.researchgate.net/publication/337228639_DEVELOPMENT_AND_EXPERIMENTAL_VALIDATION_OF_A_HALL_EFFECT_THRUSTER_RAM-EP_CONCEPT.
[26] G Koppenwallner, Satellite aerodynamics and determination of thermospheric density and wind, in: 27th International Symposium on Rarefied Gas Dynamics, 2011, URL https://doi.org/10.1063/1.3562824.
[27] J Padilla, Comparison of DAC and MONACO DSMC Codes With Flat Plate Simulation, Technical Report, NASA Langley Research Center, 2013, URL https://ntrs.nasa.gov/archive/nasa/casi.ntrs.nasa.gov/20100029686.pdf.
[28] M Young, E Muntz, J Wang, Maintaining continuous low orbit flight by using in-situ atmospheric gases for propellant, in: Rarefied Gas Dynamics: 22nd International Symposium, 2001, URL https://doi.org/10.1063/1.1407646.
[29] NASA, State of the art in small sat technology - power, 2020, URL https://www.nasa.gov/smallsat-institute/sst-soa/power.
[30] J Wertz, W Larson, Space Mission Analysis and Design, third ed., Microcosm Press/Kluwer Academic Publishers, 1999.
[31] eoPortal Directory, GOCE spacecraft, 2021, URL https://directory.eoportal.org/web/eoportal/satellite-missions/g/goce.
[32] G Cifali, et al., Experimental characterization of HET and RIT with atmospheric propellants, in: 32nd International Electric Propulsion Conference, Wiesbaden, Germany, 2011, URL http://electricrocket.org/IEPC/IEPC-2011-224.pdf.
[33] B Lotz, et al., Radio frequency ion thrusters operated with non-conventional propellants, Trudy MAI 60 (2012) URL http://trudymai.ru/eng/published.php?ID=35398&eng=Y.
[34] GMAT, General mission analysis tool, 2021, URL https://sourceforge.net/projects/gmat/.
[35] M Rosengren, Improved technique for passive eccentricity control, in: Orbital Mechanics and Mission Design; Proceedings of the AAS/NASA International Symposium, San Diego, USA, January 1989, pp. 49–58.
[36] D Brouwer, Solution of the problem of artificial satellite theory without drag, Astron. J. 64 (1959) 378, http://dx.doi.org/10.1086/107958.
[37] R Lyddane, Small eccentricities or inclinations in the Brouwer theory of the artificial satellite, Astron. J. 68 (1963) 555, http://dx.doi.org/10.1086/109179.
[38] eoPortal Directory, SLATS/Tsubame, 2021, URL https://directory.eoportal.org/web/eoportal/satellite-missions/s/slats.